Title

Clonal Dynamics in the Male Germline from Development to Next Generation

Authors

Tatsuro Ikeda[1,2,3*], Maurice Langhinrichs[2*], Tamar Nizharadze[2], Chieko Koike[1], Yuzuru Kato[4,5,6], Katsushi Yamaguchi[7], Shuji Shigenobu[4,7], Kana Yoshido[8], Shinnosuke Suzuki[1,4], Toshinori Nakagawa[1,4], Ayumi Maruyama[1], Seiya Mizuno[9], Satoru Takahashi[9], Hans-Reimer Rodewald[10], Thomas Höfer[2#], Shosei Yoshida[1,4#]

Affiliations

1. Division of Germ Cell Biology, National Institute for Basic Biology, National Institutes of Natural Sciences, Higashiyama 5-1, Myodaiji, Okazaki 444-8787, Japan

2. Division of Theoretical Systems Biology, German Cancer Research Center, Im Neuenheimer Feld 580, 69120 Heidelberg, Germany

3. Japan Society for the Promotion of Science, 5-3-1 Kojimachi, Chiyoda-ku, Tokyo 102-0083, Japan

4. Graduate Institute for Advanced Studies, SOKENDAI, Okazaki 444-8787, Japan

5. Department of Gene Function and Phenomics, Mammalian Development Laboratory, National Institute of Genetics, 1111 Mishima, Shizuoka 411-8582, Japan

6. Department of Genome Biology, Graduate School of Medicine, Osaka University, Yamadaoka 2-2, Suita 565-0871, Japan.

7. Trans-Omics Facility, National Institute for Basic Biology, National Institutes of Natural Sciences, Higashiyama 5-1, Myodaiji, Okazaki 444-8787, Japan

8. Laboratory of Theoretical Biology, Graduate School of Biostudies, Kyoto University,

Yoshidakonoecho, Sakyo, Kyoto 606-8315, Japan.

9. Laboratory Animal Resource Center in Transborder Medical Research Center, University of Tsukuba 305-8575, Japan

10. Division of Cellular Immunology, German Cancer Research Center, Im Neuenheimer Feld 280, 69120 Heidelberg, Germany

* Equal contribution

Authors for correspondence: shosei@nibb.ac.jp, t.hoefer@dkfz-heidelberg.de

Abstract

Germ cells support the continuation and evolution of species. In mammals, the germ line trajectory, originating from a small number of primordial germ cells (PGCs), has been a focal point investigated using mouse models. Yet, the precise contribution of individual PGC lineages to the adult gametes and to the next generation, a process that incubates and transmits *de novo* genetic mutations and epigenetic variability, remains enigmatic. Here, by employing a *Polylox*[1] DNA barcoding technology and mathematical modelling, we unveiled the clonal dynamics of the mouse male germline from development through adulthood and to the next generation. We found that, within cells initially specified to become germ cells in early embryogenesis, >30% of clones are lost during migration before settling at the testis, with the surviving PGC clones expanded quite unevenly. In contrast, within developing testes, in which PGCs are compartmentalised into quasi-one-dimensional seminiferous tubules, their clonal repertoire (i.e., diversity and size distribution) is preserved until adulthood. Further, the clonal repertoire in spermatogonial stem cells (SSCs) is proportionally mirrored in sperm production and in the offspring. These results advocate that early pruning and late preservation of male germ cell clones underlie the diversity and skewness of cell lineages transmitted to the next generation.

Main

The germline, distinct from the somatic lineage supporting bodily functions, is dedicated to generating gametes—sperm and eggs. Elucidating the clonal dynamics of germ cell lineage through an organism's life cycle and across generations is vital for understanding how genetic variation, including *de novo* mutations and epimutations that originate in the germline, is shaped through developmental processes and gametogenesis, and ultimately transmitted to subsequent generations. In mammals, the germline is specified in early embryos as a cluster of founder cells, termed primordial germ cells (PGCs). In mice, PGCs are specified around embryonic day (E)6.5 in the posterior extraembryonic region, migrate into the embryo proper via the hindgut, and colonise the bilateral gonads by E10.5–11.5[2,3]. In male mice, the embryonic testis microenvironment converts sexually undifferentiated PGCs to male cells called gonocytes (or prospermatogonia). Encapsulated by around eleven separate seminiferous tubules (designated as testis cords before postnatal lumenisation) composed of gonadal somatic cells called Sertoli cells[4], gonocytes divide mitotically till around E14.5, followed by cell cycle-arrest until birth[5,6]. After birth, gonocytes resume mitotic division, a fraction of which establishes the pool of spermatogonial stem cells (SSCs). SSCs, located on the basement membrane within the seminiferous tubules, persistently self-renew and support continual sperm production throughout the reproduction period[7]. While the developmental program from PGC specification to SSC establishment and differentiation into sperm has been detailed at the cell population level, it remains elusive how descendants of individual PGCs (PGC clones) contribute to SSCs, sperm, and offspring.

To elucidate the clonal dynamics of PGCs, cell lineage tracing methods have been developed and applied for germline. Classically, labelling with lysinated rhodamine

42 dextran (LRDX) revealed that a fraction of cells within E6.0–6.5 mouse embryos
43 contribute to both PGCs and extraembryonic tissues[8]. More recently, use of one or a few
44 fluorescent proteins have uncovered the heterogenous proliferation, localisation, and
45 death of PGCs at different developmental stages[9-11]. However, the limited marker
46 variations used in these studies hinder the ability to distinguish among tens to thousands
47 of PGC clones and to track them simultaneously to adulthood and the next generation.
48 To overcome this limitation, common to other developmental processes, much
49 effort has been made to develop DNA barcoding methods, with which large numbers of
50 cells could be labelled individually with diverged DNA sequences[1,12-19]. Many barcoding
51 technologies are based on CRISPR/Cas9-based gene editing, which limits the ability to
52 distinguish clonal barcodes that are most likely generated only once (within a single cell)
53 from common barcodes that have higher generation probabilities in multiple cells. By
54 contrast, the *Polylox* technology[1] can generate DNA barcodes with over 1 million
55 theoretical diversity *in vivo* based on Cre/loxP-dependent recombination, enabling
56 reliable calculation of each barcode's expected generation probability (P_{gen}) and hence
57 identification of clonal barcodes. Here, by leveraging *Polylox*, we introduced highly
58 diverse barcodes into the whole population of mouse PGCs and followed the evolution
59 of their clonal repertoire throughout from development to the next generation.
60

Tracing the PGC-clonal repertoire through development and adulthood

61 To barcode embryonic PGCs using *Polylox*, we developed a *Prdm14-Mer-iCre-*
62 *Mer* (*MiCM*) transgenic mouse line, which expresses MiCM, a strictly tamoxifen-
63 dependent Cre recombinase[20,21], under the control of the *Prdm14* regulatory region
64 (Extended Data Fig. 1a,b). *Prdm14* is an essential gene required for PGC specification

65 and germline establishment, showing specific expression in PGCs from E6.5 to E14.5[22].
66 To induce the barcodes in PGCs, we crossed male and female mice harbouring the
67 *Prdm14-MiCM* and *Polylox* transgene, respectively, to obtain doubly transgenic embryos
68 (Fig. 1a). Barcodes were found to be generated exclusively in PGCs but not in gonadal
69 somatic cells with a strict dependence on tamoxifen (4-OHT) administration to the
70 pregnant mothers (Extended Data Fig. 1c–e). Such barcoding procedure did not affect the
71 distribution and number of gonadal PGCs (Extended Data Fig. 1f,g).

72 Using this experimental system, we first analysed the clonal evolution of the
73 initially established PGCs (Fig. 1a). After 4-OHT injection into the mothers at E6.5 and
74 E6.75, germ cells and surrounding somatic tissues were collected from multiple male
75 mice at different time points. To comprehensively identify recombined barcodes and their
76 composition within the germline, we decoded all barcodes contained in the samples by
77 long-read amplicon sequencing of the *Polylox* locus (Fig. 1a, Extended Data Fig. 2a). The
78 posterior half of the embryo (including the allantois) was harvested at E8.5, and the
79 bilateral testes from E12.5 to 1 year after birth.

80 At E8.5, we detected 58.2 ± 13.8 (SD) barcodes per individual (including left
81 and right testes, N=6 mice) (Fig. 1b,c). Of note, however, the number of barcodes does
82 not directly indicate the number of PGC clones, since some common barcodes are
83 expected to occur at high probabilities and thereby introduced in multiple PGCs[1].
84 Therefore, by simulating the process of barcode generation through a random sequence
85 of recombinations, we estimated the number of PGCs that constituted the barcode
86 repertoire recovered at E8.5 to be 126.2 ± 35.2 (Extended Data Fig. 2b; Supplementary
87 Methods), consistent with the reported count of PGCs[23].

88 Interestingly, compared with E8.5, the recovered barcodes (summing from both

89 testes) were decreased at E12.5 (24.5 ± 7.6, N=13 mice) (Fig. 1b,c). Subsequently, the
90 number of barcodes became stable and maintained through puberty until one year of age
91 (Fig. 1c). The initial decline suggests a marked reduction in clonal diversity, indicating
92 that E6.5-labeled PGCs clones undergo substantial pruning during migration. Once
93 settled in the testes, however, such surviving PGC clones will persist through germline
94 development into adulthood.

95 Next, we analysed the change in the distribution of PGC clone size, i.e., the
96 number of constituent cells. To do this, we first verified that the read frequency of
97 barcodes proportionally reflects the number of cells carrying each barcode (Extended
98 Data Fig. 2c). We then focused on clonal barcodes, whose very low, computationally
99 estimated probability of generation ($P_{gen} < 0.001$, in this case) suggest their generation
100 within a single PGC. We found that the contribution of each clonal barcode recovered at
101 E8.5 was largely even, being around 1% of all barcode reads (Fig. 1d), consistent with
102 the observation that a single mouse embryo contains 116±4.4 PGCs at this stage[23].
103 However, by E12.5, when ~3,500 PGCs are found in bilateral testes (Extended Data Fig.
104 1f), the frequency of clonal barcodes became more uneven, with some expanded to about
105 10% of the total barcode reads (i.e., about 350 cells per clone) while small clones
106 occupied less than 1% (<35 cells per clone) (Fig. 1d, Extended Data Fig. 2d). In contrast,
107 after E12.5, while the total germ cell number increases greatly, the degree of uneven
108 clonal contribution remained largely unchanged during development through adulthood.

109 We further found that around 50% of clonal barcodes were shared between
110 bilateral testes harvested on E12.5 and later time points, while the other half were
111 recovered unilaterally (Extended data Fig. 2e,f). Bilaterally observed clonal barcodes
112 showed greater contributions than those found unilaterally (Extended data Fig. 2g). This

113 finding suggests that the PGC clone size variation occurs during the migration phase,
114 fairly before the PGCs split into populations to colonise the left and right testes.
115
116 **Clone size-dependent transmission to the offspring**
117 To evaluate how the uneven contribution of E6.5 PGC-derived clones is
118 reflected by the sperm production (spermatogenesis) and transmission to the next
119 generation, four E6.5-barcoded males were mated with multiple females from 2 to 10
120 months of age (Fig. 2a). These fathers were sacrificed when they reached the age of one
121 year, and the barcodes included in the FACS-sorted SSC pool and in the entire testis
122 (representing the bulk of spermatogenesis) were analysed. The results indicated that clone
123 composition in the SSC pool is proportionally reflected by spermatogenesis (Fig. 2b,
124 Extended Data Fig. 3a).
125 Then, barcodes inherited by offspring through their father's sperm were
126 determined. Each of the four fathers carrying the *Polylox* transgene heterozygously sired
127 over 200 offspring, about a half of which inherited barcodes. Sanger sequencing of
128 offspring's *Polylox* loci revealed about 20 barcodes inherited from a single father
129 (Extended Data Fig. 3b,c). Again, we found a strong linear correlation between barcode
130 frequency of fathers' SSCs and their offspring (Fig. 2c, Extended Data Fig. 3d,e).
131 Barcodes with major contributions to SSCs and spermatogenesis were frequently found
132 in offspring; those with minor contributions appeared only infrequently or never. Together,
133 compositions of E6.5-PGC clones in fathers' SSCs are directly mirrored to the sperm pool
134 and offspring, suggesting probabilistic drawings of germ cell clones in SSCs to sperm
135 and the next generation.
136 We further questioned whether the PGC clones' contribution to the sperm pool

showed any temporal drift with fathers' ageing (Extended Data Fig. 3f). However, the barcodes observed in offspring showed no apparent paternal age-dependent drift, a notion supported by mathematical simulations and statistical evaluations (Extended Data Fig. 3g,h). These results support the view that once the SSC pool is established, early PGC-derived clones continue to contribute stably and evenly to active spermatogenesis throughout the reproductive period.

Combining the observed pruning during embryonic development and subsequent lifelong preservation of clonal divergence, we conclude that the early dynamics of PGCs determines their long-term outcome in their contribution to sperm and the next generation.

Stochastic dynamics of PGC clones and prediction of a "non-arriving" fraction

Given the critical role of early clonal pruning, we quantitatively modelled the population dynamics of PGCs during development using mathematical and model-based analyses. We first found that, when rescaling all clone sizes (Fig. 1d) by the mean clone size, the cumulative distribution of scaled clone sizes x follows the simple exponential, e^{-x}, at E8.5. Importantly, this exponential distribution was observed for all subsequent time points and even across generations (Extended Data Fig. 4a,b). Remarkably, such a shape-invariant exponential distribution of mean-normalized clone sizes is a robust indicator of a neutral birth-death process, in which cells undergo stochastic division ("birth") and loss ("death"). By contrast, if a subset of PGC clones expanded under heritable and non-random selective advantages, the clone-size distribution would deviate from exponentiality, developing a heavier tail (Extended Data Fig. 4c,d). Taken together, the observed heterogeneity in PGC clone sizes can be quantitatively explained by a

161 random birth-death process, with minimal, if any, contribution from heritable selective
162 effects.

163 Motivated by the implication that PGCs follow the same stochastic rules, we
164 moved to resolve the evolution of PGC clones across successive developmental events,
165 including induction, expansion, and migration to bilateral gonads. To this end, we
166 modelled four plausible schemes based on a stochastic birth-death process. Using
167 Bayesian inference, we then evaluated the predictive capacity of each model against
168 diverse measures, including the identity and composition of recovered barcodes, barcode
169 sharing between bilateral testes, and the overall kinetics of PGC numbers between E6.5
170 and E12.5[23,24] (Extended Data Fig. 5a,b; Supplementary Methods). We found that the
171 model simulations showed a remarkably high predictive ability if cells are assumed to all
172 survive during migration but a fraction of them do not reach the testes (Model 1; Fig. 3a,b
173 and Extended Data Fig. 5a–f). Such cell loss during migration was modelled as a
174 stochastic transition to a "non-arriving PGCs" fraction, in which cells are still present at
175 least until E9.5 but will not be involved in the testis at E12.5 or contribute to subsequent,
176 definitive germline. The other three models (Models 2–4) do not simultaneously explain
177 the measurements above with realistic parameters and are therefore not supported
178 (Extended Data Fig. 5a). Thus, Model 1 not only explains the measured data but also
179 makes a testable prediction of the "non-arriving PGCs" fraction.

180 The high predictive capacity of Model 1 enabled us to simulate the clone
181 dynamics of PGCs and to infer their key quantitative properties (Fig. 3c). During early
182 migration phase, when PGC clones consist of only a few cells, stochastic cell division
183 and loss introduce random variations in clone size, estimated to range from one to >12
184 cells per clone at ~E9.5. This heterogeneity in clone size becomes proportionally fixed

185 during the subsequent expansion phase, as the influence of random division and loss
186 diminishes with increasing clone size, leading to stable PGC contributions by ~E11 (Fig.
187 3c bottom). It is also estimated that, among the initial PGCs observed at E6.5, ~68%
188 contribute to the definitive germline, with ~71% contributing bilaterally and ~29%
189 unilaterally to the testes (Extended Data Fig. 5g,h). Further, the clones with large
190 frequency at E9.5 are expected more to contribute bilaterally and to be kept still large till
191 E12.5 (Extended Data Fig. 5i), consistent with the observed relationship between clonal
192 frequency and bilaterality (Extended data Fig. 2g).
193

194 **Identification and characterisation of the predicted non-arriving PGC fraction**

195 Our modelling analysis predicts that a significant fraction of PGCs become
196 "non-arriving", failing to settle in the testis and thus not contributing to the definitive
197 germline. We then experimentally tested this prediction and investigated the cellular
198 identity of "non-arriving" cells. One possibility is that, while initiating the PGC program,
199 some cells may eventually differentiate into somatic lineages. This scenario is consistent
200 with previous studies of cells expressing *Blimp1* and *Dppa3* using co-immunostaining,
201 transplantation, and Cre-driven reporter analyses[25,26]. In addition, some PGCs may not
202 migrate properly to the gonads by E10.5 and are eventually eliminated, as observed
203 previously[27,28].

204 To characterize the cells that had expressed *Prdm14* at E6.5 *in vivo*, we labelled
205 them with GFP using *CAG-CAT-EGFP* reporter[29], instead of *Polylox* (Fig. 3d). Following
206 4-OHT injection at E6.5 and E6.75, we observed GFP-labelled cells exclusively in an
207 extraembryonic region adjacent to the posterior tip of the epiblast at E7.5 (Fig. 3e),
208 consistent with the reported PRDM14 expression at this stage[22]. We found that some

209 GFP-positive cells were negative for OCT4, another marker of PGCs (Fig. 3e, Extended
210 Data Fig. 5j). Notably, at E8.5, ~52% (125/239) of GFP^+ cells were $OCT4^+$ and located
211 anteriorly near the hindgut, while the other ~48% (114/239) were $OCT4^-$ and located
212 posteriorly on the allantois (Fig. 3f, Extended Data Fig. 5j). Within the GFP^+OCT4^- cells,
213 ~69% (36/52) expressed extraembryonic mesoderm marker FOXF1[30] (Extended Data Fig.
214 5k).

215 Our barcoding experiments reveal that, among the descendants of *Prdm14*$^+$
216 presumptive PGCs at E6.5, only about half establish the definitive germline, whereas the
217 remainder adopt somatic fates. This is consistent with the view that PGCs commit to the
218 germline only after colonising the gonads, under the influence of gonadal signals and
219 DAZL expression[31-33]. In line with this, recent single-cell analyses indicate that *Prdm14*$^+$
220 cells constitute common precursors of PGCs and extraembryonic mesoderm, whose PGC
221 potential becomes progressively restricted as their BMP responsiveness increases[34].
222 Together, these complementary findings converge on a coherent scheme in which a subset
223 of *Prdm14*$^+$ cells establish the definitive germline by activating a core set of germline-
224 identity genes (including *Prdm14*, *Oct4*, *Blimp1*, *Tcfap2c*, and *Dppa3*)[3], as they migrate
225 into the embryonic gonads.

226 From a perspective of clonal dynamics, such refinement of PGCs associates
227 with significant loss and unequal expansion of surviving clones. We speculate that such
228 a selective process during this early phase may play a role in establishing the integrity of
229 germ cell population for their future production of functional gametes.

230

231 **Turnover of gonocyte sub-clones within parental PGC clones**

232 Having observed a marked stabilisation of PGC clone dynamics in later stages,

233 we next turned to this phase of slower clonal evolution. As detailed, after colonisation in
234 the testis, the composition of E6.5-labeled PGC clones remained stable from the late
235 embryogenesis through postnatal and adult stages, with individual clone sizes increasing
236 in parallel with the overall germ cell population[31]. However, while these "parental clones"
237 persisted as a whole, it remained unknown whether the constituent "sub-clones" were
238 proportionally maintained or instead subject to loss and expansion.

239 To address this question, we barcoded the gonocytes at E11.5 and analysed the
240 composition of recovered barcodes at subsequent time points (Fig. 4a). We found that the
241 barcode number decreased from E12.5 (416 ± 171 per individual) to 1 week after birth,
242 around which SSCs are established (242 ± 50) (Fig. 4b). Following this period, the
243 number of recovered barcodes remained stable until 1 year old. Focusing on clonal
244 barcodes (P_{gen} < 0.00003; indicating single gonocyte-derived sub-clones), we estimated
245 that the fraction of sub-clones surviving from embryonic to adult stages is ~50%
246 (Extended Data Fig. 6). Further, at E12.5 and E13.5, contributions of individual clonal
247 barcodes were relatively even around 0.03%, which became diverged by 1 week after
248 birth and maintained until one year old (Fig. 4c).

249 These findings indicate that, in contrast to the high stability of the "parental"
250 PGC clones, their "sub-clones" undergo loss and expansion during the late embryonic
251 and perinatal periods. Interestingly, although the E11.5-labelled sub-clones became stable
252 during adulthood, it is established that adult SSC-derived clones (i.e., "sub-sub-clones")
253 also undergo loss and replacement during homeostasis[35,36]. This highlights a hierarchical
254 mode of clonal dynamics, in which stabilisation occurs at higher levels, while continual
255 turnover persists at lower levels.

256

Segregated spatial distribution of PGC clones in seminiferous tubules

PGCs migrate through embryonic tissues and settle in the testes as a sparse population. Across this transition into the testis, germ cells experience a drastic change in tissue architecture, which could underlie the stabilisation of clone dynamics. By E13.5, PGCs are incorporated into ~11 distinct testis cords (Extended Data Fig. 1g). These cords develop into seminiferous tubules through postnatal lumenisation, ultimately extending up to 2 meters in total length per testis in adults[4,37,38]. Through this process, germ cells are confined within a distinct, quasi-one-dimensional tubular geometry, which may restrict clonal intermixing.

To gain insight into the relevance of such compartmentalisation, we examined the spatial distribution of germline clones within seminiferous tubules. Following barcoding at E6.5, all seminiferous tubules from two testes, each derived from different adult male mice, were collected in fragments ranging from 1 to 13 cm in length (Fig. 4d). Strikingly, tubule fragments, whether long (~10 cm) or short (<4 cm), contained only a minor subset of the collective barcode repertoire, typically 2–7 barcodes (Fig. 4e, Extended Data Fig. 7a–c). Furthermore, sub-fragments cut from longer fragments tended to share a common set of barcodes (Extended Data Fig. 7d). These findings reflect how clonal intermixing is limited within seminiferous tubules.

Modelling the PGC clone behaviour through testis development and homeostasis

Then, to quantitatively capture how PGC clones behave within seminiferous tubules, we extended our previous model into adulthood by incorporating the tubular anatomical configuration (Fig. 5a, Extended Data Fig. 8). In this scheme, at E12.5, germ cells were segregated and aligned within a one-dimensional arrangement of ~11

281 seminiferous tubules, which elongated unevenly[37] until 2 weeks after birth when Sertoli
282 cells ceased proliferation[39,40] (Extended Data Fig. 8d); SSC population expanded in
283 proportion to the tubule elongation till this stage and then remained constant. We also
284 incorporated the observed ~50% loss of the E11.5-labeled PGC sub-clones (Extended
285 Data Fig. 6) and the previously reported stochastic neighbour turnover of SSCs during
286 homeostatis[36] (Supplementary Methods).

287 In this modelling scheme, we found that the spatial arrangement of the clones
288 in later stages was strongly influenced by their distribution upon their
289 compartmentalisation into forming testis cords at E12.5. Therefore, we explored the most
290 plausible spatial arrangements—from complete mixing to various local patch
291 structures—by comparing simulated and observed barcode distributions in long and short
292 fragments of adult seminiferous tubules (Fig. 4e, Extended Data Fig. 7, 8a–c). The
293 observed limited barcode diversity in long fragments indicates that individual PGC clones
294 showed restricted contribution to only a subset of the eleven seminiferous tubule loops.
295 However, intriguingly, a simple contiguous allocation of each clone within a single tubule
296 does not explain the comparable barcode numbers included in short and long fragments.
297 Instead, our modelling infers a locally repetitive patch structure, where alternating PGC
298 clones form small patches containing ~150 SSCs on average, capturing all key
299 experimental observations (Fig. 5b, Extended Data Fig. 8a,b,d,e).

300 To experimentally assess the model-predicted clone distribution patterns, we
301 visualized E6.5 PGC clones 4-5 weeks after birth, using *Confetti*, a multi-colour
302 fluorescent protein reporter[41], instead of *Polylox* (Fig. 5c top). With very low
303 recombination efficiencies, coloured germ cells were detected in the testes of 5 out of 9
304 mice, 3 of which showed only a single colour (Extended Data Fig. 9a), suggesting that

305 cells marked by the same colour belong to a single, or a very few, PGC clones. In these
306 samples, cells of a particular colour formed clustered patches separated by unlabelled
307 cells, confined to restricted regions within a limited subset of seminiferous tubules (Fig.
308 5c, Extended Data Fig. 9b,c). This spatial pattern aligns well with the model prediction,
309 further supporting our modelling scheme for germ cell behaviour during testis
310 development.
311

312 **Tubular geometry and population effects stabilise germline clonal dynamics**

313 Consistent with observations, our model mimicking the seminiferous tubule
314 geometry stably maintained the germ cell clones over extended periods. Extrapolation to
315 2 years predicted only minimal changes in clone numbers and patch-length distributions
316 (Extended Data Fig. 10a,b). Thus, we finally examined the mechanisms underlying the
317 long-term stabilisation of germ cell clones in this model.

318 To assess the contribution of tubular tissue geometry to this property, we
319 compared clonal dynamics across models with different geometries. In addition to a truly
320 one-dimensional (1D) model, we implemented a quasi-one-dimensional (q-1D)
321 cylindrical model[36] and a global competition model, in which any cell in the population
322 can compensate for loss regardless of position (Fig. 5d; Extended Data Fig. 10c).
323 Interestingly, the global clone number and size distribution are stable with only very little
324 difference, regardless of the model geometry (Extended Data Fig. 10d,e). This supports
325 that early developmental clone size expansions not only fix the clonal germ cell
326 composition but also buffer against continued intraclonal loss during later development
327 and adult homeostasis. On the other hand, we found that the local patch composition
328 shows drastic change depending on the geometry (Fig. 5d and Extended Data Fig. 10f–

329 h). Tubular geometries (1D and q-1D) effectively enhance the stability of E11.5-labeled
330 sub-clones (Extended Data Fig. 10i) and preserve the mosaic patch structure over the
331 murine life span.

332 In conclusion, we successfully reproduced the lifetime clonal dynamics of
333 mouse male germline from PGC specification to gonad colonisation, followed by
334 compartmentalisation with mixing to testis cords and continuous turnover during tubular
335 extension and adult homeostasis. Our model proposes that developmental germ cell
336 expansion (a "population effect") and the tubular geometry support clonal stability at the
337 global and local levels.

338

339 **Discussion**

340 By integrating *Polylox* barcoding with mathematical modelling, we achieved an
341 otherwise inaccessible bird's-eye view of the clonal fate dynamics of the mouse germline
342 through development, spermatogenesis, and inheritance to offspring (Fig. 5e). Nascent
343 PGC clones undergo pronounced pruning and size divergence during migration from the
344 extraembryonic region to the embryonic gonads. In contrast, once colonising the testis,
345 the surviving PGC clones acquire remarkable stability, which persists through late
346 embryogenesis, SSC establishment, spermatogenesis, and transmission to the next
347 generation.

348 The observations in this study highlight hierarchical dynamics of germ cell
349 clones' extinction and expansion. Nascent PGC clones (i.e., E6.5-barcoded) initially
350 exhibit pruning and diversification, which become stable and preserved after settling in
351 the testis. Whereas gonocyte-derived clones (e.g., E11.5-barcoded; "sub-clones" of

352 "parental PGC clones") also show pruning and diversification until 1 week after birth,
353 when SSCs are established, then become stabilised. Similarly, during adulthood, our
354 previous studies showed that SSC-derived clones (labelled with GFP at 3 months old;
355 “sub-clones” of gonocytes-derived clones and “sub-sub-clones” of PGC-derived clones)
356 exhibit continual loss and the survivors’ expansion[35,36]. Similar short-term pruning and
357 long-term persistence likely occur continuously, beyond the time points we measured. In
358 such hierarchical dynamics, an upper clone remains while the lower clones are pruned,
359 because the former only disappears if all constituent lower clones are eliminated, an event
360 that rarely happens.

361 Although such hierarchical clonal pruning and expansion continue, their
362 dynamics change markedly before and after colonisation of the embryonic testis codes.
363 We would emphasize that the transition from dynamic to stable clone behaviour may be
364 linked with the germline's mission to transmit genomic and non-genomic information to
365 subsequent generations. In the early migratory phase, clone pruning could underpin the
366 nascent PGCs to establish the definitive germline traits, through encouraging selective
367 survival of the fittest cells. The subsequent stabilisation, enabled by a population effect
368 and the tubular geometry, may be vital for preserving clonal diversity within the germline.
369 This combined process prevents clonal dominance beyond the variation established by
370 neutral dynamics during pruning, ensuring no single clone dominates the sperm pool.

371 The limited domination of a small number of germ cell clones contrasts with
372 other somatic tissues with distinct tissue architectures. For example, in epithelial tissues,
373 in which many interfaces between competing clones appear within the extended 2D

374 geometry, clones carrying precancerous mutation are known to often expand considerably
375 with age[42]. More strikingly, in haematopoiesis, being reliant on motile stem cells over a
376 3D niche architecture of bone marrow, limited numbers of stem cell clones may
377 eventually dominate with ageing, a phenomenon designated as clonal haematopoiesis,
378 from which malignant clones could emerge to cause leukaemia[43]. Generally, domination
379 by clones accumulating precancerous and other *de novo* mutations may be undesirable.
380 However, in somatic tissues, these could be allowed if they do not affect the tissue
381 function or form tumours. In the germline context, however, mutations harmless to
382 spermatogenesis could pose significant risks to offspring's somatic tissues. Indeed, some
383 identified *de novo* mutations, while enhancing the fitness of SSC clones in the testis, cause
384 genetic disorders when transmitted to the next generation[44]. It is tempting to speculate
385 that the germline dynamics of early pruning and late preservation identified here may
386 effectively limit the dominance of mutated clones and hence their contribution to the next
387 generation.

388 In conclusion, by applying DNA barcoding technology, this study provides a
389 comprehensive and quantitative analysis of clone dynamics of the male germline from
390 development to offspring. Further advancements in barcoding and other analytical tools
391 are poised to deepen our understanding of germline lineage dynamics and its regulation.
392 Such progress is crucial for elucidating how germ cells balance high productivity, fidelity,
393 and variability, a fundamental yet unresolved question in germ cell biology.

394

395

396 ## Methods

397 **Mice.** *Rosa26*^{Polylox}[1], *CAG-CAT-EGFP*[29], *Dppa3-ECFP*[45], and *Rosa26*^{Confetti}[41] alleles were
398 previously described; *Prdm14-MiCM* allele was newly generated in this study, as detailed
399 in the following section. All these mouse lines were maintained in a C57BL/6J
400 background (purchased from CLEA Japan or Japan SLC). The *Prdm14-MiCM* transgenic
401 mice were generated with approval by Institutional Animal Experiment Committee of the
402 University of Tsukuba. All other animal experiments were approved by Institutional
403 Animal Care and Use Committee of the National Institutes of Natural Sciences.

404

405 **Generation of a *Prdm14-MiCM* transgenic allele.** A bacterial artificial chromosome
406 (BAC) carrying a genome fragment of C57BL/6J mouse spanning the entire *Prdm14*
407 coding sequence plus 157kb flanking sequence (clone RP24-341H14)[22,46] was modified
408 in *E. coli* (Extended Data Fig. 1a). Briefly, exons 2 to 5 of the *Prdm14* gene were replaced
409 by a *Mer-iCre-Mer*[20,21] sequence, polyA signal and the FRT-flanked Neo cassette, using
410 RED recombination system[47] .The LoxP and Lox511 sites on the vector were replaced
411 with *Amp*^{r} and *Zeo*^{r} genes, respectively. Finally, the Neo cassette was deleted by a
412 transient flippase activation. The resultant, *Prdm14-MiCM* BAC was purified, linearized
413 by PI-SceI digestion, and injected into pronuclei of C57BL/6J mouse zygotes to generate
414 transgenic animals. For G_0 animals, the presence of transgene was examined by PCR
415 using Taq DNA polymerase (Bioacademia) for 5min at 94°C; (20s at 94°C, 20s at 68–
416 61°C, 7s at 72°C) 8 times with 1°C touchdown; (20s at 94°C, 20s at 60°C, 7s at 72°C) 27
417 times; 14s at 72°C, with primers *MiCM_3UTR_5For* (5'-
418 GCTTATCGACTAATCAGCCATAC -3') and *Prdm14_3arm_MidRev* (5'-
419 CCACCTCACTAAGTTGCTGC-3'), amplifying 336bp sequence of the transgene. For

420 F1 and F2 generations, the transgene copy number was quantified by qPCR using
421 THUNDERBIRD SYBR qPCR Mix (Toyobo) and LightCycler 96 (Roche), for 95°C at
422 60s; (15s at 95°C, 60s at 40°C) 45 times, with primers *Prdm14_qPCR_5For* (5'-
423 CGTTTCGCTAAACTCCTTGG -3') and *Prdm14_qPCR_5Rev* (5'-
424 TGCAGCCGAGATAGGAGAAG -3') annealing Intron 1 of *Prdm14*, and *b-actin For*
425 (5'- ACCACAGGCATTGTGATGG -3') and *b-actin_Rev* (5'-
426 TCGGTCAGGATCTTCATGAGG -3') as a reference. A transgenic allele with the
427 highest copy numbers at a single locus (line #14) was selected and maintained
428 homozygously (Extended Data Fig. 1b).
429
430 **4OH-tamoxifen administration to pregnant mothers.** A stock solution of 4OH-
431 tamoxifen (Sigma-Aldrich) was prepared by dissolving 25mg 4OH-tamoxifen, as well as
432 12.5mg progesterone (Sigma-Aldrich) to sustain pregnancy, into 250µl EtOH and then
433 2250µl peanut oil (Sigma-Aldrich), using a sonication water bath, and stored at -30℃
434 until use. Male and female mice homozygously carrying the *Prdm14-MiCM* and the
435 *Polylox* alleles, respectively, were crossed to avoid leaky recombination in zygotes due
436 to maternally-derived MiCM protein accumulated in oocytes during oogenesis. After
437 overnight pair housing, a vaginal plug was checked the following morning, with midday
438 on the day of plug detection designated as E0.5. To induce at E6.5&6.75, two successive
439 doses of 150 µl stock solution (containing 1.5 mg 4OH-tamoxifen) were orally
440 administered at a 6h interval. For E11.5 induction, a dose of 100µl of stock solution
441 (containing 1mg 4OH-tamoxifen) was administered orally. For a postnatal sampling of
442 the testes, a Caesarean section was performed at E19.5, and the pups were bred by foster
443 mothers (ICR).

444

445 **PGC count.** To count the number of PGCs with and without barcoding, homozygous
446 *Polylox* females were crossed with males carrying *Prdm14-MiCM* and *Dppa3-ECFP*
447 alleles to conceive embryos with *Polylox*, *Prdm14-MiCM,* and *Dppa3-ECFP* alleles
448 heterogeneously. Testes of these embryos with, at E6.5&E6.75 or E11.5, or without 4OH-
449 tamoxifen administration were harvested at E12.5 and fixed in 4% PFA in PBS for 2h at
450 4°C. The samples were washed with PBST, blocked with 4% Donkey serum in PBST at
451 RT for 3h, incubated with primary antibody solution [rabbit anti-DDX4 (Abcam
452 Cat#ab13840, 0.05%) supplemented with 4% donkey serum in PBST] at 4°C overnight,
453 washed with PBST at RT for >1h four times, and incubated in 2nd antibody solution
454 [donkey anti-Rabbit IgG (H+L) Cy3 (Jackson ImmunoResearch 711-165-152, 0.1%) and
455 goat anti-GFP (SICGEN AB0020-200) conjugated with DyLight™ 488 NHS Ester
456 (Thermo Fisher Scientific, 0.1%), supplemented with 4% donkey serum in PBST] at 4°C
457 overnight. After washing with 1mL PBST at RT for >1h four times, the testis samples
458 were mounted with Scale SQ[48], and serial images were acquired for 3D reconstruction
459 using TCS-SP8 (Leica). To count the number of PGCs automatically, captured images
460 were analysed by custom program written for R software environment (www.r-
461 project.org) with EBImage packages[49]. In brief, PGC masks were created using ECFP
462 and immunostained DDX4 signals by applying Gaussian blur filter followed by local
463 thresholding and size selection. Information of each single PGC across several slices was
464 integrated.

465

466 **General procedure for barcode sequencing, decoding, and filtering.**

467 The *Polylox* locus was PCR-amplified from genomic DNA samples using primers #2,427

468 and #2,450[1,50] and KOD Fx Neo polymerase (Toyobo) with a thermal cycler MiniAmp
469 Plus (Thermo Fisher Scientific) under a thermal cycling condition of initial denaturation
470 (94°C for 2 min) followed by 28 or 30 cycles of 98°C for 10 sec, 64°C for 30 sec, and
471 68°C for 150 sec, and a final extension (68°C for 7 min). The amplicons were purified by
472 AMPure XP (Beckman Coulter) and proceeded for library preparation using a
473 SMRTbell® Express Template Prep Kit 2.0 (Pacific Biosciences) according to the
474 manufacturer's protocol (101-791-700), and long-read Single Molecule, Real-Time
475 (SMRT) sequencing using Sequel I and Sequel IIe sequencers (Pacific Biosciences) with
476 standard parameters.

477 The obtained circular consensus sequencing (CCS) reads were converted to
478 barcodes, followed by classifying into 'legitimate' barcodes (those which are theoretically
479 possible to occur from the original *Polylox* sequence) and 'illegitimate' barcodes (those
480 which are expected not to occur), as described previously[1,50]. Given the rarity of
481 illegitimate barcode detection and their distinct read number distribution from the vast
482 majority of legitimate barcodes, we reason that these anomalous barcodes likely arose
483 from PCR or bioinformatics processing errors, rather than from genuine recombination
484 events involving the *Polylox* locus within germ cell genomes. This suggests that
485 legitimate barcodes may include some artefacts, so we filtered out rarely observed
486 barcodes altogether so that the illegitimate barcode reads became less than 5% of total
487 reads (Extended Data Fig. 2a).

488

489 **Specificity verification of barcode introduction into PGCs.** Triple transgenic embryos
490 carrying *Polylox*, *Prdm14-MiCM* and *Dppa3-ECFP* alleles resulting from the crossing
491 described previously were barcoded by 4OH-tamoxifen administration at E6.5&6.75 or

492 E11.5. For each schedule, gonads collected from eight embryos at E13.5 were pooled and
493 dissociated by a Liberase solution [0.5 mg/mL DNase (Worthington), 0.26 U/mL
494 Liberase™ TM (Roche), and 18U /mL Britase (Wako) in PBS]. PGCs and gonadal
495 somatic cells were separately collected as $ECFP^+$ and $ECFP^-$ fractions, respectively, using
496 a MA900 cell sorter (Sony), and proceeded for genome PCR amplification (30 cycles)
497 and barcode analysis as described above. We found that recombined barcodes were
498 detected only in the $ECFP^+$ fraction sorted from the testes of embryos obtained from 4OH-
499 tamoxifen injected mothers, with no recombination detected at all in the $ECFP^-$ fraction
500 or samples without 4OH-tamoxifen injection, verifying that barcode recombination
501 occurred in a high germ cell-specific and tamoxifen-dependent manner (Extended Data
502 Fig. 1e).
503
504 **Barcode analysis of developing and adult germ cells.** To observe the clonal dynamics
505 during development, embryos carrying *Polylox* and *Prdm14-MiCM* alleles were barcoded
506 at E6.5&6.75 or E11.5, followed by harvesting posterior-half embryos at E8.5 (for
507 E6.5&6.75-labeled embryos only) or bilateral testes at time points spanning from E12.5
508 to 1Y. Samples harvested at embryonic stages, i.e., posterior-half embryos and testes after
509 removing the mesonephros, were lysed separately in 16μl protease solution; all the
510 template DNA was directly used for PCR amplification (28 cycles) and barcode analyses.
511 Postnatally, right and left testes were independently collected, removed off the tunica
512 albuginea, lysed in 200–1000μl protease solution followed by DNA purification, and
513 100–1000 ng template DNA (representing 1.7×10^4–10^5 cells) was used for barcode PCR
514 amplification (28–30 cycles) and barcode analysis. To calculate the barcode compositions
515 per individual, barcode reads from bilateral testes were combined based on the

516 assumption that the germ cell numbers were equal between testes.

517 We found that ~4% of these double-transgenic mice harboured recombined
518 barcode sequences broadly over somatic cells, likely due to leaky and 4OH-tamoxifen-
519 independent recombination during very early development. Accordingly, barcode
520 sequencing was performed on samples taken from individuals whose somatic tissues
521 (head or tail, respectively, for samples taken at E8.5 or other stages) were confirmed by
522 PCR amplification to have full-length *Polylox* sequences only. Further, the sex of the E8.5
523 and E12.5 embryos were determined by PCR amplification of the *Rbm31x/y* genes[51].

524

525 **Verification that the barcode reads linearly reflect the cell composition.**

526 Considering the possibility of biased PCR-amplification, library construction and
527 sequencing, we verified if and how much the composition of the barcode reads mirrors
528 that of cells carrying heterogeneous barcodes. Testes from adult mice barcoded at
529 E6.5&6.75 were dissociated by a Liberase solution (see above), and were incubated in
530 antibody solution [Alexa Fluor 647-conjugated rat anti-CD9 (Biolegend 124810, 1:500,
531 PECy7-conjugated rat anti-KIT (Biolegend 105814, 1:200) and Brilliant Violet 421-
532 conjugated rat anti-CD324 (Biolegend 147319, 1:1000) in PBS] on ice for 30 min. Then,
533 a $CDH1^{+}/CD9^{+}/KIT^{-}$ undifferentiated spermatogonia fraction was collected by an
534 MA900 cell sorter (Sony), as a bulk of 17,000 to 25,000 cells and in parallel as a separate
535 assembly of hundreds of individual cells. Barcode analyses through PCR-amplification
536 and amplicon long-read sequencing were conducted as described previously. In parallel,
537 barcodes are also decoded separately in individual cells by Sanger sequencing (Fasmac)
538 of the *Polylox* sequence amplified by nested PCR. The primers used are #2,450 and #494
539 for the first round, and #2,426 and #2,427 for the second round, respectively[1]. Both

540 rounds of PCR were performed using KOD Fx Neo at 25µl scale and the following
541 protocol: 2 min at 94°C followed by 25 rounds of (10s at 98°C, 30s at 64°C, 2min30sec
542 at 68°C) and 7min at 68°C. 1µl of the 1st PCR product was used as a template for the 2nd
543 PCR. The products of the second PCR were treated with ExoSAP-IT Express (Thermo
544 Fisher Scientific) and were sequenced with primers #2,427, #2,450, #2,623 (5′-
545 AGAAGTTGCATACACAGTATTG-3′) or #2,622 (′-
546 ATCATCGAGCTCGTCAACAATG-3′)[1]. A custom script
547 (SangerSeqSingleFilesAnalysis.m from Daniel Postrach) was used to determine barcode
548 elements in sequencing reads.
549 We found a strong linear correlation between the frequency of barcode reads
550 obtained from the bulk population using deep sequencing and the number of cells whose
551 barcode was individually determined (Extended Data Fig. 2c). We concluded that the
552 barcode frequencies obtained from bulk Sequel deep sequencing faithfully reflect the
553 composition of cell numbers with these barcodes within the population of interest and
554 that the technical biases, if any, are negligible.
555
556 **Comparison of barcode distributions between the SSC pool, spermatogenesis, and**
557 **offspring.** Four male mice barcoded at E6.5&6.75 were each crossed with multiple ICR
558 females from 8–9 weeks old. Because the males heterozygously harboured the *Polylox*
559 transgene, about half of the offspring inherited barcodes via sperm. The fathers were
560 sacrificed at 1 year of age, whose right and left testes were separately dissociated using a
561 Liberase solution (see above). Half of the dissociated cells were used to FACS-sort a
562 "SSCs" (i.e., $CDH1^{+}CD9^{+}KIT^{-}$ undifferentiated spermatogonia) fraction, while the other
563 half were directly proceeded as "spermatogenesis" fraction without sorting, for amplicon

564 sequencing as described previously to gain barcode reads. In parallel, the offspring's tail
565 tips were digested by Cica Genius AN (Kanto Chemical) to prepare the DNA, followed
566 by PCR-amplification of the *Polylox* sequence using KOD Fx Neo with the temperature
567 condition of 2 min at 94°C followed by 32 rounds of (10s at 98°C, 30s at 64°C, 2min30sec
568 at 68°C) and 7min at 68°C, using primers #2,427 and #2,450. PCR products were treated
569 with ExoSAP-IT Express (Thermo Fisher Scientific) and barcodes were sequenced in the
570 same way as single-cell-derived barcodes (see above). Temporal bias of barcode
571 appearance in offspring was examined using the methods detailed in the Supplementary
572 Methods.
573
574 **Visualization of *Prdm14*$^{+}$ cell clones using a fluorescence reporter.** To visualize the
575 spatial distribution of the descendants of cells expressing *Prdm14* at E6.5&6.75,
576 homozygous *CAG-CAT-EGFP* females were crossed with homozygous *Prdm14-MiCM*
577 males to conceive embryos carrying *Prdm14-MiCM* and *CAG-CAT-EGFP* alleles
578 heterozygously. Following 4OH-tamoxifen administration to pregnant mothers at
579 E6.5&6.75, whole embryos and posterior-half embryos were harvested at E7.5 and E8.5,
580 respectively, and fixed in 4% PFA in PBS for 2h at 4°C. After washing with PBS
581 containing 0.1% TritonX-100 (PBST), the samples were blocked with 4% Donkey serum
582 in PBST containing 0.1% Hoechst 33342 (Thermo Fisher Scientific) and incubated for
583 3h at room temperature (RT). Then, the blocking solution was switched to the primary
584 antibody solution [anti-GFP (goat, Sicgen AB0020-200; rat, Nacalai Tesque 04404-84; or
585 chicken, Aves Labs GFP-1010), rabbit anti-OCT4 (Abcam ab181557), with or without
586 goat anti-FoxF1 (R&D Systems AF4798); all at 0.1%; supplemented with 4% donkey
587 serum in PBST], and the samples were incubated at 4°C overnight (>16h). Afterwards,

588 samples were washed with PBST at RT for >1h four times, and incubated in the secondary
589 antibody solution [any one of anti-Goat IgG (H+L) Alexa 488 (705-545-147), anti-Rat
590 IgG (H+L) Alexa 488 (712-545-153) or anti-Chicken IgY (H+L) Alexa 488 (703-545-
591 155), together with anti-Rabbit IgG (H+L) Cy3 (711-165-152); all donkey-derived, from
592 Jackson ImmunoResearch, and used in 0.1%; supplemented with 4% donkey serum in
593 PBST] at 4°C overnight. After washing with PBST at RT for >1h four times, the samples
594 were mounted using Scale SQ[48] and serial images were acquired for 3D reconstruction,
595 using a TCS-SP8 confocal microscope (Leica).
596
597 **Barcode analysis of seminiferous tubule fragments.** To address the spatial distribution
598 of barcoded clones over seminiferous tubules, the testes of two E6.5&6.75-barcoded male
599 mice were obtained at 8–9 weeks of age. For each mouse, one of the testes was lysed for
600 barcode amplicon sequencing as described earlier to verify the degree of recombination;
601 the other was extensively disentangled to collect virtually the entire seminiferous tubule
602 length in as long fragments as possible. Fragments 4cm or longer were cut into sub-
603 fragments. Genomic DNA purified from each of these (sub)fragments was used for
604 amplicon-sequencing to determine the barcode composition included therein. For each
605 fragment, barcodes with <1% read frequency were filtered out because they were likely
606 due to contaminated germ cells from other fragments during sampling. To estimate the
607 length of tubule segments occupied by cells with each barcode, its read frequency was
608 multiplied by the length of the fragments from which the barcode was yielded. The
609 number of SSCs in each fragment was estimated by multiplying its length by 30 cells per
610 millimeter[52].
611

612 **Multi-colour reporter observation of PGC clones in seminiferous tubules.**
613 Homozygous *Rosa26*^{Confetti} females were crossed with homozygous *Prdm14-MiCM* males
614 to obtain foetus that obtain both genes heterozygously. After 4OH-tamoxifen
615 administration at E6.5&6.75 and Caesarean section as in the same way with barcoding
616 procedure, seminiferous tubules of bilateral testes obtained from males between 29 and
617 36 days old were untangled thoroughly and fixed in 4% PFA in PBS for 1h at 4°C.
618 Followed by washing with PBST, the fluorescent images of seminiferous tubules were
619 obtained using a M165FC stereoscopic microscope (Leica) with GFP-LP, RFP-LP and
620 ET-CFP filters. Green signals were regarded as cYFP but not nGFP according to their
621 localisation in the cytoplasm. We could not find an ECFP signal, possibly because the
622 mECFP cassette was not activated by recombination or the mECFP signal was not strong
623 enough to be distinguished from background signals. Because we found clear cYFP and
624 cRFP signals in only limited areas in 5 out of 9 mice (Extended Data Fig. 9a), we reasoned
625 that recombination occurred infrequently and labelled cells derived from only one or a
626 few PGCs at E6.5&E6.75.
627
628 **Mathematical modelling of clonal PGC dynamics.** Methods and theory for the
629 modelling of clonal PGC dynamics are detailed in Supplementary Methods and
630 Supplementary Equations. In brief, we modelled cellular dynamics of division, migration,
631 loss and spatial organisation following clones of the emerging E6.5 PGCs. Simulated
632 PGC clones were probed with *Polylox* recombination, to infer key biological insights
633 from multiple aspects of the barcoding data. Namely, the reduction of clonal diversity in
634 the embryo, followed by the maintenance of the survivors, and the spatial organisation of
635 these clones in the testes over the murine life span. We investigated mechanism for the

postnatal stability of PGC clones, incorporating the specific geometry of the seminiferous tubules in the testes.

Code availability. All code for mathematical modelling was written in the Julia programming language and is available on GitHub. The complete executing code for clonal PGC dynamics is contained in GermlineDynamics (https://github.com/hoefer-lab/GermlineDynamics). Code therein calls methods for *Polylox* barcode simulation and inference from the package PolyloxMechanics.jl (https://github.com/hoefer-lab/PolyloxMechanics.jl). All Bayesian inferences are based on methods from the package ABCdeZ.jl (https://github.com/hoefer-lab/ABCdeZ.jl). During the review process 'GermlineDynamics' and 'PolyloxMechanics.jl' (as of now private repositories) are available at https://tsbnc.dkfz.de/index.php/s/TODO_ADD_LINK (Password: TODO_ADD_PW). The custom programs used for counting the number of PGCs, and all the other calculations for plotting written as R markdown documents, are available upon request.

Data availability. All barcode CCS data are archived in DDBJ Sequence Read Archive (DRA) and are available upon peer-reviewed publication. All Sanger sequence reads are also available upon peer-reviewed publication. The image datasets are available at SSBD:repository upon peer-reviewed publication.

Acknowledgements

We thank the members of the NIBB Yoshida lab, the DKFZ Höfer lab, and N. Honda for discussion, NIBB Model Organisms Facility for animal care, NIBB Trans-Omics Facility for Sequel sequencing, T. Feyerabend for a *Rosa26*^{Polylox} mouse strain, M. Saitou, K. Hayashi and G. Nagamatsu for a *Dppa3-ECFP* mouse strain, M. Saitou, H. Ohta and K. Kurimoto for a BAC clone, K. Busch and M. Reth for a *Mer-iCre-Mer* construct, and X. Wang, J. Rößler and D. Postrach for scripts to determine *Polylox* barcodes.

Funding

This work is funded by MEXT and JSPS (Grant-in-Aid for Scientific Research KAKENHI JP25114004, JP15K21736, JP17K19413, JP18H05551, and JP23H04952 to S.Y.; and JP17H07335, JP19J00410, JP21K15111, JP22H05639, JP24H01413, and JP24K18129 to T.I.), and AMED (AMED-ASPIRE, 25jf0126012h0001 and 26jf0126012h0002 to S.Y.). TI was supported by the JSPS Research Fellowship for Young Scientists (JP19J00410). M.L. was supported by the Helmholtz Graduate School for Cancer Research fellowship. T.H. was supported by Sonderforschungsbereich (SFB 873-B11).

Author contributions

T.I. performed most of the experiments, with the support of C.K. and A.M.; T.I., M.L., and T.Ni. performed barcode calculations and statistical evaluations; M.L. designed and performed mathematical modelling of clonal/barcode dynamics, with input from T.Ni. and T.H.; Y.K. developed an algorithm to count PGCs; K.Ya. and S.Sh. performed SMRT sequencing and initial data mining; M.L. and K.Yo. performed time-series mathematical

682 analysis of barcode appearance in offspring; T.I., S.Su. and T.Na. conducted cell sorting;
683 S.M. and S.T. established a *Prdm14-MiCM* by microinjection; T.I. and S.Y. designed the
684 experiments; T.I., M.L., T.H., and S.Y. wrote the manuscript with input from all
685 contributors; S.Y., H.-R.R., and T.H. conceived and supervised the study.
686

687 **Author information**

688 These authors contributed equally: Tatsuro Ikeda, Maurice Langhinrichs
689

690 **Competing interests**

691 These authors declare no competing interests.
692

693 **Additional information**

694 Supplementary Information is available for this paper.
695 Correspondence and requests for materials should be addressed to Thomas Höfer and
696 Shosei Yoshida.
697

References

698 1 Pei, W. *et al.* Polylox barcoding reveals haematopoietic stem cell fates realized in
699 vivo. *Nature* **548**, 456-460 (2017). https://doi.org/10.1038/nature23653
700 2 Molyneaux, K. & Wylie, C. Primordial germ cell migration. *Int J Dev Biol* **48**,
701 537-544 (2004). https://doi.org/10.1387/ijdb.041833km
702 3 Saitou, M. & Yamaji, M. Primordial Germ Cells in Mice. *Csh Perspect Biol* **4**
703 (2012). https://doi.org/10.1101/cshperspect.a008375
704 4 Combes, A. N. *et al.* Three-dimensional visualization of testis cord
705 morphogenesis, a novel tubulogenic mechanism in development. *Dev Dyn* **238**,
706 1033-1041 (2009). https://doi.org/10.1002/dvdy.21925
707 5 Western, P. S., Miles, D. C., van den Bergen, J. A., Burton, M. & Sinclair, A. H.
708 Dynamic regulation of mitotic arrest in fetal male germ cells. *Stem Cells* **26**, 339-
709 347 (2008). https://doi.org/10.1634/stemcells.2007-0622
710 6 Nagano, R. *et al.* Reproliferation and relocation of mouse male germ cells
711 (gonocytes) during prespermatogenesis. *Anat Rec* **258**, 210-220 (2000).
712 https://doi.org/10.1002/(SICI)1097-0185(20000201)258:2<210::AID-
713 AR10>3.0.CO;2-X
714 7 Yoshida, S. Heterogeneous, dynamic, and stochastic nature of mammalian
715 spermatogenic stem cells. *Curr Top Dev Biol* **135**, 245-285 (2019).
716 https://doi.org/10.1016/bs.ctdb.2019.04.008
717 8 Lawson, K. A. & Hage, W. J. Clonal Analysis of the Origin of Primordial Germ-
718 Cells in the Mouse. *Ciba F Symp* **182**, 68-84 (1994).
719 https://doi.org/10.1002/9780470514573.ch5
720 9 Ueno, H., Turnbull, B. B. & Weissman, I. L. Two-step oligoclonal development

721 of male germ cells. *Proc Natl Acad Sci U S A* **106**, 175-180 (2009).
722 https://doi.org/10.1073/pnas.0810325105
723 10 Nguyen, D. H. *et al.* Apoptosis in the fetal testis eliminates developmentally
724 defective germ cell clones. *Nat Cell Biol* **22**, 1423-+ (2020).
725 https://doi.org/10.1038/s41556-020-00603-8
726 11 Lei, L. & Spradling, A. C. Mouse primordial germ cells produce cysts that
727 partially fragment prior to meiosis. *Development* **140**, 2075-2081 (2013).
728 https://doi.org/10.1242/dev.093864
729 12 McKenna, A. *et al.* Whole-organism lineage tracing by combinatorial and
730 cumulative genome editing. *Science* **353**, aaf7907 (2016).
731 https://doi.org/10.1126/science.aaf7907
732 13 Raj, B. *et al.* Simultaneous single-cell profiling of lineages and cell types in the
733 vertebrate brain. *Nat Biotechnol* **36**, 442-450 (2018).
734 https://doi.org/10.1038/nbt.4103
735 14 Pei, W. *et al.* Resolving Fates and Single-Cell Transcriptomes of Hematopoietic
736 Stem Cell Clones by PolyloxExpress Barcoding. *Cell Stem Cell* **27**, 383-395 e388
737 (2020). https://doi.org/10.1016/j.stem.2020.07.018
738 15 Kalhor, R. *et al.* Developmental barcoding of whole mouse via homing CRISPR.
739 *Science* **361** (2018). https://doi.org/10.1126/science.aat9804
740 16 Alemany, A., Florescu, M., Baron, C. S., Peterson-Maduro, J. & van Oudenaarden,
741 A. Whole-organism clone tracing using single-cell sequencing. *Nature* **556**, 108-
742 112 (2018). https://doi.org/10.1038/nature25969
743 17 Spanjaard, B. *et al.* Simultaneous lineage tracing and cell-type identification using
744 CRISPR-Cas9-induced genetic scars. *Nat Biotechnol* **36**, 469-473 (2018).

745 https://doi.org/10.1038/nbt.4124

746 18 Bowling, S. *et al.* An Engineered CRISPR-Cas9 Mouse Line for Simultaneous
747 Readout of Lineage Histories and Gene Expression Profiles in Single Cells. *Cell*
748 **181**, 1693-1694 (2020). https://doi.org/10.1016/j.cell.2020.06.018

749 19 Li, L. *et al.* A mouse model with high clonal barcode diversity for joint lineage,
750 transcriptomic, and epigenomic profiling in single cells. *Cell* **186**, 5183-5199
751 e5122 (2023). https://doi.org/10.1016/j.cell.2023.09.019

752 20 Busch, K. *et al.* Fundamental properties of unperturbed haematopoiesis from stem
753 cells in vivo. *Nature* **518**, 542-546 (2015). https://doi.org/10.1038/nature14242

754 21 Zhang, Y. *et al.* Inducible site-directed recombination in mouse embryonic stem
755 cells. *Nucleic Acids Res* **24**, 543-548 (1996). https://doi.org/10.1093/nar/24.4.543

756 22 Yamaji, M. *et al.* Critical function of Prdm14 for the establishment of the germ
757 cell lineage in mice. *Nat Genet* **40**, 1016-1022 (2008).
758 https://doi.org/10.1038/ng.186

759 23 Seki, Y. *et al.* Cellular dynamics associated with the genome-wide epigenetic
760 reprogramming in migrating primordial germ cells in mice. *Development* **134**,
761 2627-2638 (2007). https://doi.org/10.1242/dev.005611

762 24 Tam, P. P. L. & Snow, M. H. L. Proliferation and Migration of Primordial Germ-
763 Cells during Compensatory Growth in Mouse Embryos. *J Embryol Exp Morph*
764 **64**, 133-147 (1981). https://doi.org/10.1242/dev.64.1.133

765 25 Mikedis, M. M. & Downs, K. M. STELLA-positive subregions of the primitive
766 streak contribute to posterior tissues of the mouse gastrula. *Dev Biol* **363**, 201-218
767 (2012). https://doi.org/10.1016/j.ydbio.2011.10.003

768 26 Mikedis, M. M. & Downs, K. M. PRDM1/BLIMP1 is widely distributed to the

769 nascent fetal-placental interface in the mouse gastrula. *Dev Dynam* **246**, 50-71
770 (2017). https://doi.org/10.1002/dvdy.24461
771 27 Runyan, C. *et al.* Steel factor controls midline cell death of primordial germ cells
772 and is essential for their normal proliferation and migration. *Development* **133**,
773 4861-4869 (2006). https://doi.org/10.1242/dev.02688
774 28 Stallock, J., Molyneaux, K., Schaible, K., Knudson, C. M. & Wylie, C. The pro-
775 apoptotic gene Bax is required for the death of ectopic primordial germ cells
776 during their migration in the mouse embryo. *Development* **130**, 6589-6597 (2003).
777 https://doi.org/10.1242/dev.00898
778 29 Kawamoto, S. *et al.* A novel reporter mouse strain that expresses enhanced green
779 fluorescent protein upon Cre-mediated recombination. *Febs Lett* **470**, 263-268
780 (2000). https://doi.org/10.1016/s0014-5793(00)01338-7
781 30 Mahlapuu, M., Ormestad, M., Enerback, S. & Carlsson, P. The forkhead
782 transcription factor Foxf1 is required for differentiation of extra-embryonic and
783 lateral plate mesoderm. *Development* **128**, 155-166 (2001).
784 https://doi.org/10.1242/dev.128.2.155
785 31 Gill, M. E., Hu, Y. C., Lin, Y. & Page, D. C. Licensing of gametogenesis,
786 dependent on RNA binding protein DAZL, as a gateway to sexual differentiation
787 of fetal germ cells. *Proc Natl Acad Sci U S A* **108**, 7443-7448 (2011).
788 https://doi.org/10.1073/pnas.1104501108
789 32 Hu, Y. C. *et al.* Licensing of primordial germ cells for gametogenesis depends on
790 genital ridge signaling. *PLoS Genet* **11**, e1005019 (2015).
791 https://doi.org/10.1371/journal.pgen.1005019
792 33 Nicholls, P. K. *et al.* Mammalian germ cells are determined after PGC

793 colonization of the nascent gonad. *Proc Natl Acad Sci U S A* **116**, 25677-25687
794 (2019). https://doi.org/10.1073/pnas.1910733116
795 34 Hadas, R. *et al.* Temporal BMP4 effects on mouse embryonic and extraembryonic
796 development. *Nature* **634**, 652-661 (2024). https://doi.org/10.1038/s41586-024-
797 07937-5
798 35 Nakagawa, T., Nabeshima, Y. & Yoshida, S. Functional identification of the actual
799 and potential stem cell compartments in mouse spermatogenesis. *Dev Cell* **12**,
800 195-206 (2007). https://doi.org/10.1016/j.devcel.2007.01.002
801 36 Klein, A. M., Nakagawa, T., Ichikawa, R., Yoshida, S. & Simons, B. D. Mouse
802 germ line stem cells undergo rapid and stochastic turnover. *Cell Stem Cell* **7**, 214-
803 224 (2010). https://doi.org/10.1016/j.stem.2010.05.017
804 37 Nakata, H. *et al.* Three-dimensional structure of seminiferous tubules in the adult
805 mouse. *J Anat* **227**, 686-694 (2015). https://doi.org/10.1111/joa.12375
806 38 Clermont, Y. H., C. Microscopic anatomy of the sex cords and seminiferous
807 tubules in growing and adult male albino rats. *American Journal of Anatomy* **108**,
808 79–97 (1961). https://doi.org/10.1002/aja.1001080106
809 39 Vergouwen, R. P. *et al.* Postnatal development of testicular cell populations in
810 mice. *J Reprod Fertil* **99**, 479-485 (1993). https://doi.org/10.1530/jrf.0.0990479
811 40 Vergouwen, R. P. F. A., Jacobs, S. G. P. M., Huiskamp, R., Davids, J. A. G. &
812 Derooij, D. G. Proliferative Activity of Gonocytes, Sertoli Cells and Interstitial-
813 Cells during Testicular Development in Mice. *J Reprod Fertil* **93**, 233-243 (1991).
814 https://doi.org/10.1530/jrf.0.0930233
815 41 Snippert, H. J. *et al.* Intestinal crypt homeostasis results from neutral competition
816 between symmetrically dividing Lgr5 stem cells. *Cell* **143**, 134-144 (2010).

817 https://doi.org/10.1016/j.cell.2010.09.016

818 42 Martincorena, I. Somatic mutation and clonal expansions in human tissues.
819 *Genome Med* **11**, 35 (2019). https://doi.org/10.1186/s13073-019-0648-4

820 43 Jaiswal, S. & Ebert, B. L. Clonal hematopoiesis in human aging and disease.
821 *Science* **366** (2019). https://doi.org/10.1126/science.aan4673

822 44 Goriely, A. & Wilkie, A. O. Paternal age effect mutations and selfish
823 spermatogonial selection: causes and consequences for human disease. *Am J Hum*
824 *Genet* **90**, 175-200 (2012). https://doi.org/10.1016/j.ajhg.2011.12.017

825 45 Ohinata, Y., Sano, M., Shigeta, M., Yamanaka, K. & Saitou, M. A comprehensive,
826 non-invasive visualization of primordial germ cell development in mice by the
827 Prdm1-mVenus and Dppa3-ECFP double transgenic reporter. *Reproduction* **136**,
828 503-514 (2008). https://doi.org/10.1530/Rep-08-0053

829 46 Yamaji, M. *et al.* PRDM14 ensures naive pluripotency through dual regulation of
830 signaling and epigenetic pathways in mouse embryonic stem cells. *Cell Stem Cell*
831 **12**, 368-382 (2013). https://doi.org/10.1016/j.stem.2012.12.012

832 47 Lee, E. C. *et al.* A highly efficient Escherichia coli-based chromosome
833 engineering system adapted for recombinogenic targeting and subcloning of BAC
834 DNA. *Genomics* **73**, 56-65 (2001). https://doi.org/10.1006/geno.2000.6451

835 48 Hama, H. *et al.* Sca/eS: an optical clearing palette for biological imaging. *Nat*
836 *Neurosci* **18**, 1518-+ (2015). https://doi.org/10.1038/nn.4107

837 49 Pau, G., Fuchs, F., Sklyar, O., Boutros, M. & Huber, W. EBImage--an R package
838 for image processing with applications to cellular phenotypes. *Bioinformatics* **26**,
839 979-981 (2010). https://doi.org/10.1093/bioinformatics/btq046

840 50 Pei, W. *et al.* Using Cre-recombinase-driven Polylox barcoding for in vivo fate

841 mapping in mice. *Nat Protoc* **14**, 1820-1840 (2019).
842 https://doi.org/10.1038/s41596-019-0163-5
843 51 Tunster, S. J. Genetic sex determination of mice by simplex PCR. *Biol Sex Differ*
844 **8** (2017). https://doi.org/10.1186/s13293-017-0154-6
845 52 Kitadate, Y. *et al.* Competition for Mitogens Regulates Spermatogenic Stem Cell
846 Homeostasis in an Open Niche. *Cell Stem Cell* **24**, 79-+ (2019).
847 https://doi.org/10.1016/j.stem.2018.11.013
848 53 Royer, L. A. *et al.* ClearVolume: open-source live 3D visualization for light-sheet
849 microscopy. *Nat Methods* **12**, 480-481 (2015).
850 https://doi.org/10.1038/nmeth.3372
851 54 Nakagawa, T. *et al.* A multistate stem cell dynamics maintains homeostasis in
852 mouse spermatogenesis. *Cell Rep* **37**, 109875 (2021).
853 https://doi.org/10.1016/j.celrep.2021.109875
854 55 Kanatsu-Shinohara, M., Naoki, H. & Shinohara, T. Nonrandom Germline
855 Transmission of Mouse Spermatogonial Stem Cells. *Dev Cell* **38**, 248-261 (2016).
856 https://doi.org/10.1016/j.devcel.2016.07.011
857 56 Bailey, N. T. J. *The elements of stochastic processes with applications to the*
858 *natural sciences*. (Wiley, 1964).
859 57 Klein, A. M. & Simons, B. D. Universal patterns of stem cell fate in cycling adult
860 tissues. *Development* **138**, 3103-3111 (2011). https://doi.org/10.1242/dev.060103
861 58 Heathcote, C. R. & Moyal, J. E. The Random Walk [in Continuous Time] and Its
862 Application to the Theory of Queues. *Biometrika* **46**, 400-411 (1959).
863 https://doi.org/10.1093/biomet/46.3-4.400

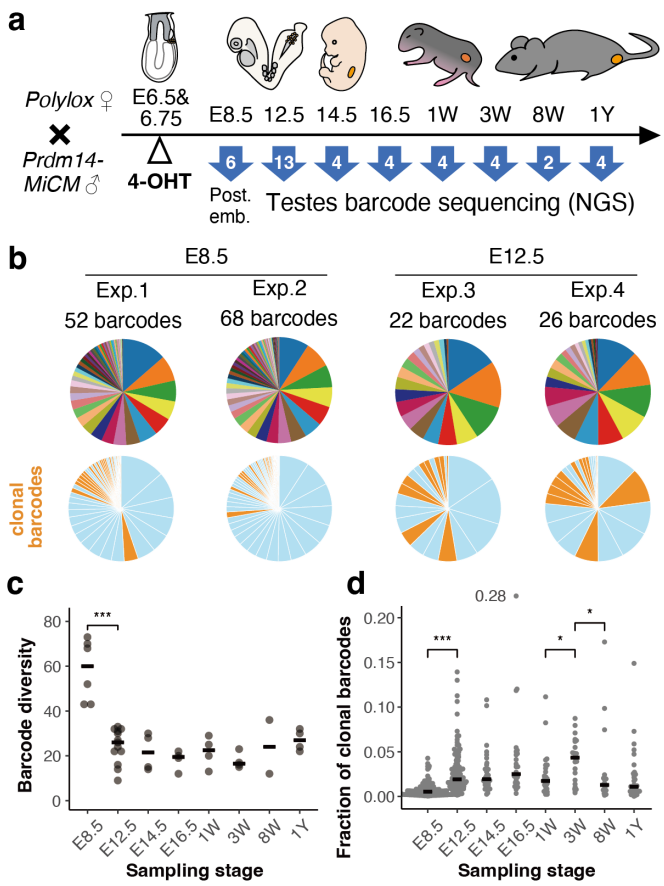

Figure 1. Barcode analysis of E6.5&6.75-labeled PGC clones

a, Experimental overview. *Prdm14-MiCM*;*Polylox* male embryos were barcoded at E6.5&6.75, whose barcodes in germline were analysed at the indicated time points from individuals of indicated numbers shown in arrows. The barcode reads obtained from the testes of 1Y-old mice were from experiments detailed in Fig. 2.

b, Representative distribution of barcode reads found in two embryos each at E8.5 and E12.5, displayed in pie charts. Unrecombined barcodes are excluded. Orange highlighted in lower pie charts indicates "clonal barcodes", whose generation probability P_{gen} are low (<0.001), enough to be postulated to be introduced in a single PGC.

c, Barcode diversity found in individual mice (grey dots).

d, The contribution of individual clonal barcodes (P_{gen}<0.001) in all recombined barcodes recovered from each mouse. In (**c**) and (**d**), values only between neighbouring time points were statistically evaluated. Horizontal bars indicate medians. ***p<0.001, *p<0.05, Mann-Whitney-Wilcoxon test (MWW).

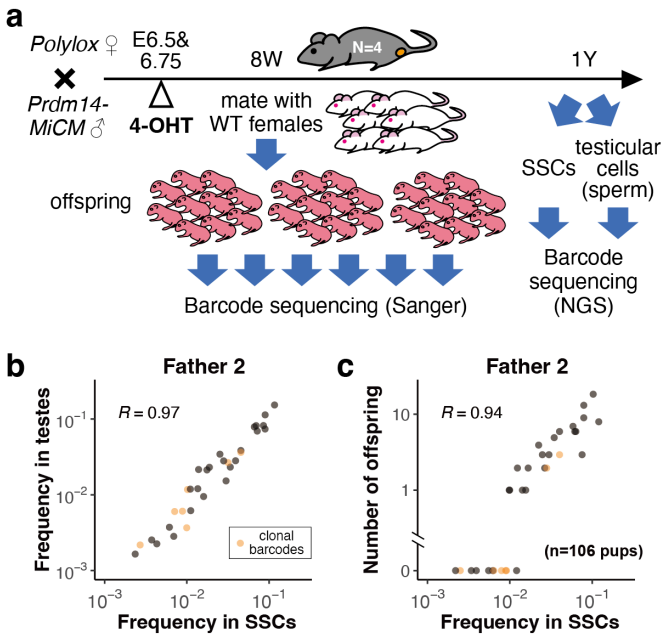

Figure 2. Barcode transmission from SSCs through spermatogenesis to offspring

a, Experimental overview. Four *Prdm14-MiCM*;*Polylox* male mice barcoded at E6.5&6.75 were repeatedly mated with multiple females to give rise to a substantial number of offspring till 1Y old. Barcodes transmitted into offspring were determined individually by Sanger sequencing. Then, the fathers were sacrificed and the barcodes included in their SSCs (specifically, undifferentiated spermatogonia) and bulk testicular cells (representing active spermatogenesis) were analysed by deep-sequencing. Given the heterozygosity of the fathers, approximately half embryos inherit the barcodes. **b**,**c**, Correlation between barcode compositions in SSCs and the bulk testes (**b**), and between father's SSCs and the 106 offspring that harboured barcodes (**c**). Representative data obtained from one male mouse (Father 2) are indicated; see Extended Data Fig. 3 for those from the other fathers. For SSCs and bulk testis, barcodes from each of the bilateral testes were summed with a 1:1 ratio. "Clonal

barcodes" (P_{gen}<0.001) are highlighted in orange. In (**c**), actual number of offspring with barcodes are indicated. Spearman correlation coefficients are indicated.

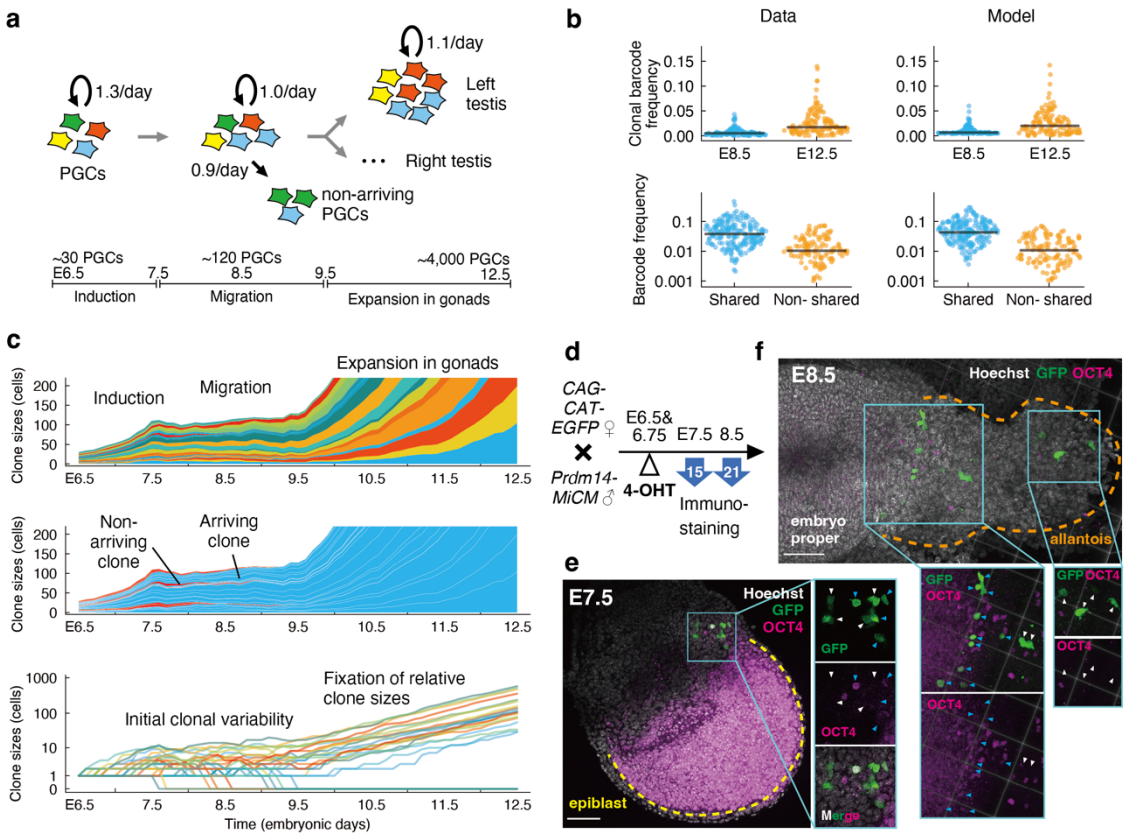

Figure 3. Inference of clonal dynamics of PGCs from E6.5 to E12.5

a, Scheme of the "top model" with parameters inferred from E6.5&6.75 PGC-barcoding data. In this scheme, the initial ~30 PGC clones proliferate through sequential phases of neutral birth-death processes, reaching the left and right gonads at expanded clone sizes. During the migration phase (E7.5–9.5) a non-arriving fraction of PGCs emerges that lost the ability to reach the gonads. The class of birth-death processes was informed by rescaled clone size distributions (Extended Data Fig. 4; Supplementary Methods). Different models were tested and fitted on barcode, cell number and sharing statistics, among which this top model was found to be best-fit (Extended Data Fig. 5a).

b, Predictive capacity of the top model (right) for a dataset not used for fitting (left). The frequency of clonal *Polylox* barcodes among all recombined barcodes for both

measurement time points (top panels; model shows a representative simulation). Barcode frequencies (all except unrecombined) at E12.5 distinguishing barcodes shared and non-shared between bilateral testes (bottom panels). Horizontal lines indicate medians.

c, Model prediction of the clonal dynamics of PGCs. Model inference was conducted based on *Polylox* barcodes, followed by re-simulations for individual clones originating from a single cell at E6.5. Clone size dynamics of the re-simulated ~30 PGC clones were shown in different colours (top panel), arriving (blue) and non-arriving (red) clones (middle panel). Clone size evolution plotted on log-scale (bottom panel), indicating that early stochastic fluctuation in clone size become stabilised by ~E11, after which clones expanded proportionally.

d, Experimental overview for (**e**) and (**f**). Following induction by 4-OHT administration at E6.5&6.75, GFP-labelled cells in *Prdm14-MiCM*;*CAG-CAT-EGFP* embryos were analysed at E7.5 and E8.5 for their distribution and marker protein expression.

e,**f**, E7.5 (**e**) and E8.5 (**f**) embryos, immunostained for GFP (green) and OCT4 (magenta) proteins, cyan and white arrowheads indicating $GFP^{+}OCT4^{+}$ and $GFP^{+}OCT4^{-}$ cells, respectively. Epiblast (**e**) and allantois (**f**) are outlined. In (**f**), images were 3D-visualised using ClearVolume[53]. Scale bar, 100μm.

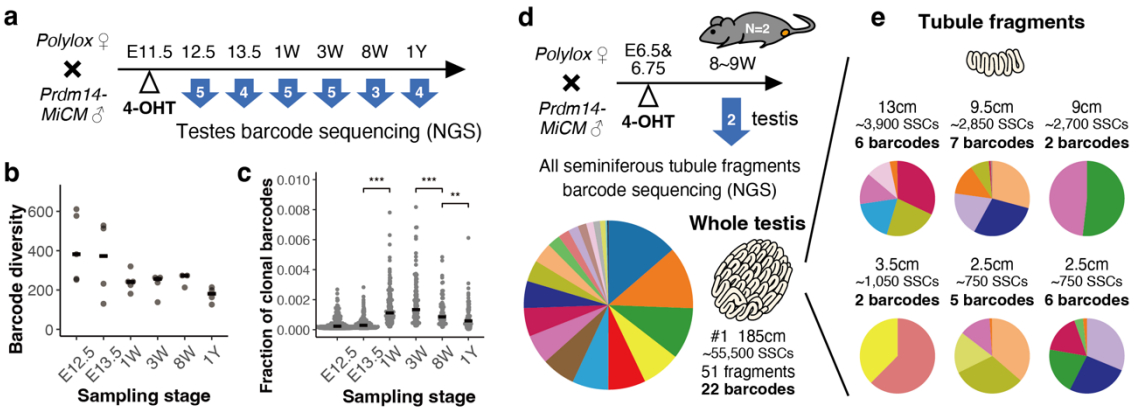

Figure 4. Barcode analysis after late induction and in fragments of seminiferous tubules

a, Experimental overview. *Prdm14-MiCM*;*Polylox* male embryos were barcoded at E11.5, whose barcodes in germline were analysed at the indicated time points from individuals of indicated numbers shown in arrows.

b, Barcode diversity found in individual mice. Horizontal bars indicate medians. No significant changes were detected between nearby stages (MWW).

c, The contribution of individual clonal barcodes (P_{gen}<0.00003) in all recombined barcodes recovered from each mouse. ***p<0.001, **p<0.01, MWW. Horizontal bars in (**b**) and (**c**) indicate medians.

d, Experimental overview is shown in top. Testis from each of the two adult *Prdm14-MiCM*;*Polylox* mice (8~9W old) induced at E6.5&6.75 were decapsulated to collect all the fragments of seminiferous tubules. Then, barcodes in all the dozens of collected fragments were read individually, compiled to reconstruct their composition over an entire testis, and summarized in a pie chart (see Method for detail).

e, Examples of long and short tubule fragments obtained in (**d**), with barcode reads therein. In (**d**) and (**e**), same colour among pie charts indicates same barcode. See Ext.

Data Fig. 7 for full dataset for this and the second testis. Estimated SSC numbers in each fragment shown (see Methods).

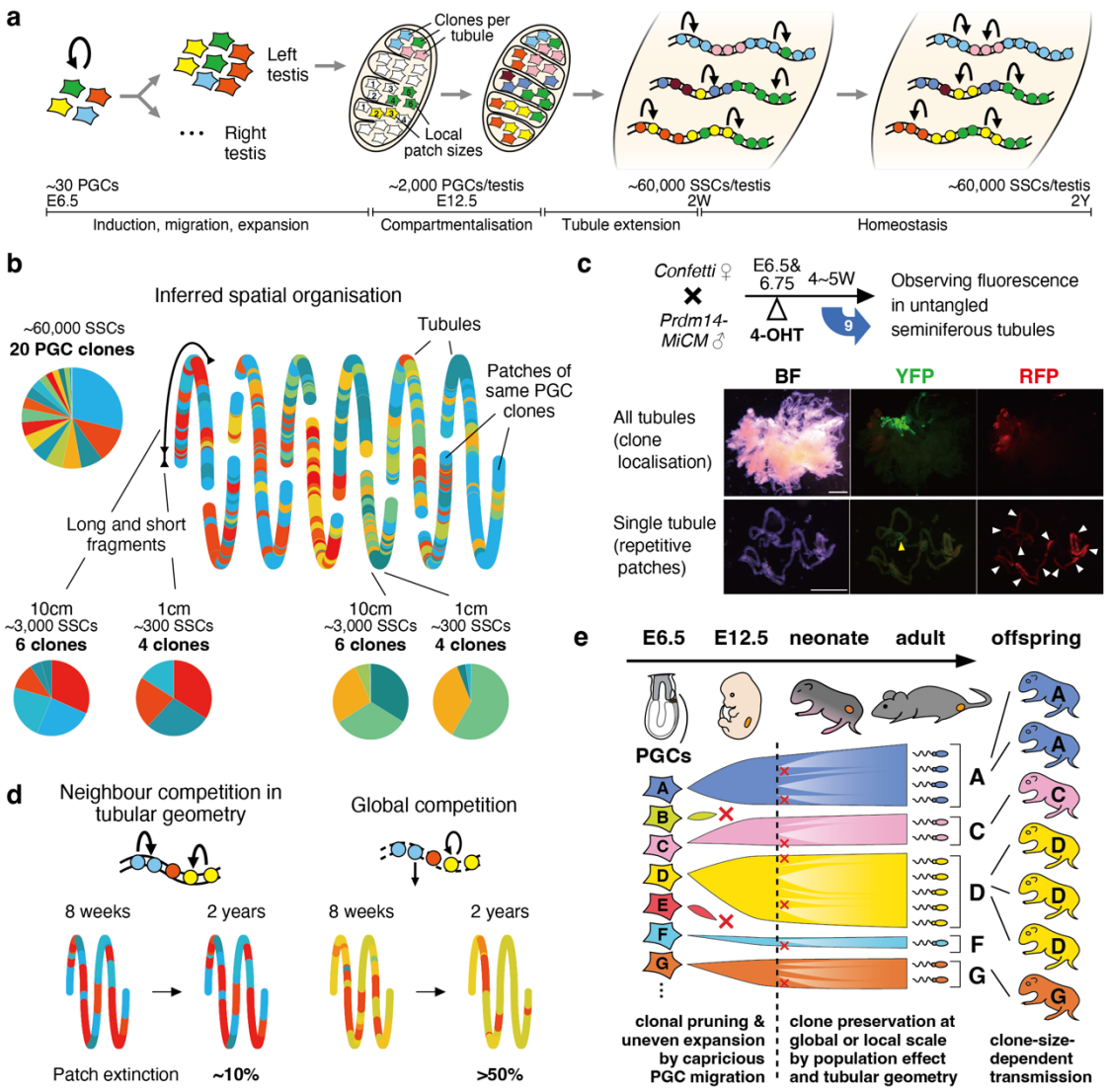

Figure 5. Modelling the lifetime clonal dynamics of male germline

a, Scheme for modelling the lifetime dynamics of the ~30 initial PGC clones at E6.5. Following the modelling over early phases till E12.5 (Fig. 3), additional models were developed to capture the germline fate behaviour over extended times, including the compartmentalisation into newly formed testis cords (E12.5), seminiferous tubule extension till 2W, and persistent homeostasis from 2W to 2Y of age. See Supplementary Methods in detail.

b, A typical example of the inferred spatial organisation of E6.5 PGC clones at 8 weeks after birth, simulated using the sequential model summarized in (**a**). Within a single testis containing ~60,000 SSCs, 20 PGC clones survived and were distributed across 11 separate tubule loops. These clones were not evenly distributed; rather, each tubule loop harboured only a subset of clones. The clones formed a mixed, repetitive patchwork structure in which short segments contained a disproportionately large number of PGC clones (e.g., 4 clones in a 1-cm segment), compared to long segments (e.g., 6 clones in a 10-cm segment), consistent with experimental observations (Fig. 4d,e and Extended Data Fig. 7).

c, Visualization of PGC clone distribution using the *Confetti* multi-fluorescence lineage reporter. Experimental design (top). Fluorescence images (middle and bottom) of gently untangled whole seminiferous tubules from a single testis of a *Prdm14-MiCM;Confetti* mouse barcoded at E6.5&6.75 (2-3m Right), harbouring large YFP^+ and RFP^+ patches (middle), or a dissected tubule fragment (2-3m tubule 4) containing a small YFP^+ patch and a cluster of non-contiguous RFP^+ patches, indicated by yellow and white arrowheads, respectively (bottom). Scale bar, 2 mm.

d, Model prediction of the lifetime dynamics of local patches under different modes of adult homeostatic regulation. In the neighbour competition model (left), which incorporates the geometry of seminiferous tubules, local patch lengths remain highly stable with a minimal patch extinction over 2 years life span. In contrast, a hypothetical global competition model with the same differentiation output but agnostic of spatial geometry (right) shows a pronounced disintegration of the local patch structure.

e, A schematic diagram summarizing the clonal dynamics of mouse male germline from development to the next generation.

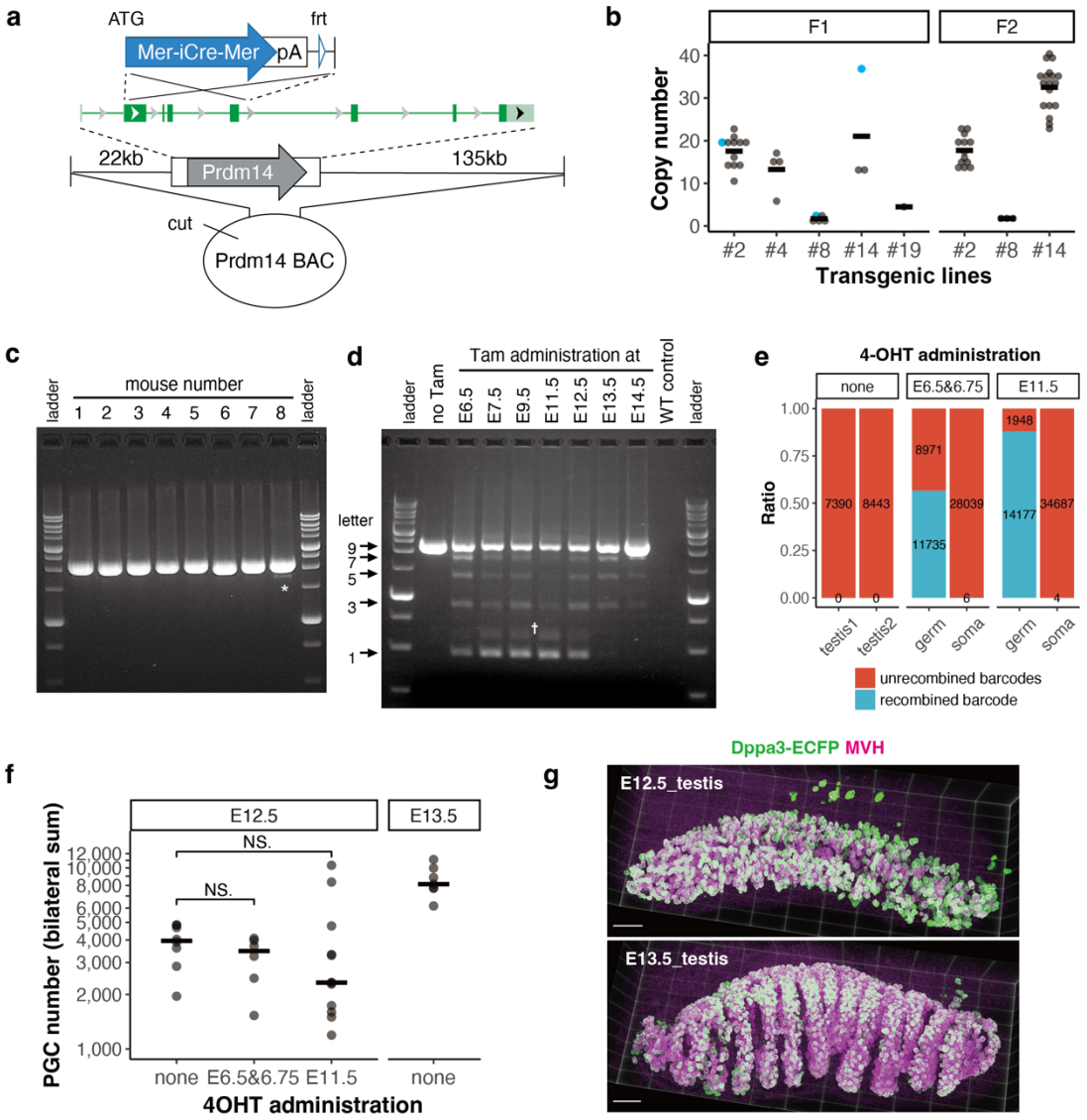

Extended Data Figure 1. Generation of *Prdm14-MiCM* transgenic alleles

a, Design of the *Prdm14-MiCM* BAC plasmid used for generating the *Prdm14-MiCM* transgenic allele, in which exons 2 to 5 was replaced by *Mer-iCre-Mer* CDS and a poly(A) addition signal.

b, Copy number of the *Prdm14-MiCM* transgene in independent multiple lines, measured by genomic qPCR. Horizontal bars indicate means. The F_1 individuals coloured in cyan were backcrossed to obtain the F_2 offspring. Given the largely

unchanged copy number between F_1 and F_2 generation, these transgenes were highly expected to be integrated in a single locus in lines #2, #8, and #14.

c, PCR-amplification of the *Polylox* locus from the tail DNA of *Prdm14-MiCM;Polylox* mice with 4OH-tamoxifen (4-OHT) administration at E6.5&6.75, showing predominant amplification of 9-letter length fragments. The lane with asterisk incudes a shorter amplified band (7-letters), likely due to a leaky recombination in early embryos. 3 out of 74 mice (4%) with or without tamoxifen administration showed such recombined short fragment(s) in tail DNA, which were excluded from subsequent analyses.

d, Representative examples of the PCR-amplified barcode sequences from testes of 3-weeks-old mice, which have received tamoxifen administration at different developmental time points as indicated. The amplified fragments with five lengths, corresponding to the 9, 7, 5, 3, and 1 letters, indicate that homologous recombination occurred between the loxP sequences contained in the *Polylox* sequence, as expected. Consistent with the expression window of Prdm14, prominent recombination was observed between E6.5 and E13.5. Dagger indicates an unidentified fragment around 600bp, which were informatically excluded from the analysis. Mice that received no tamoxifen showed no evidence of barcode recombination.

e, Verification of tamoxifen-dependent and germ cell-specific barcode induction. Testes from 3-weeks-old *Prdm14-MiCM*;*Polylox* mice without 4-OHT administration contained no recombined barcodes (left). The actual numbers of Sequel sequence reads are indicated on each coloured bar. *Prdm14-MiCM*;*Polylox;Dppa3-ECFP* triple transgenic embryos were induced by 4-OHT administration to mothers at E6.5&6.75 or E11.5 (middle and right). Then, germ cells ($ECFP^+$) and gonadal somatic cells ($ECFP^–$) were FACS-sorted from pools of gonadal cell suspension prepared from eight E12.5

embryos obtained from a single litter (2 males and 6 females for E6.5&6.75; 3 males and 5 females for E11.5). Recombined barcodes were detected exclusively in the germ cell fraction (i.e., PGCs), consolidating that recombined barcodes in gonads have derived specifically from germ cells.

f, The total number of PGCs, summed from the bilateral testes of *Prdm14-MiCM*;*Polylox*;*Dppa3-ECFP* mice, at E12.5 (with or without 4-OHT administration) and E13.5 (without 4-OHT administration). PGCs were counted based on immunostaining of Dppa3-ECFP and DDX4, and image analysis of encircled nuclei (see Methods). Horizontal bars indicate medians. No statistical significance was detected (MWW).

g, 3D-representative images of E12.5 and E13.5 testes, in which PGCs were immuno-stained for Dppa3-ECFP and DDX4, using ClearVolume[53]. Scale bar, 100μm.

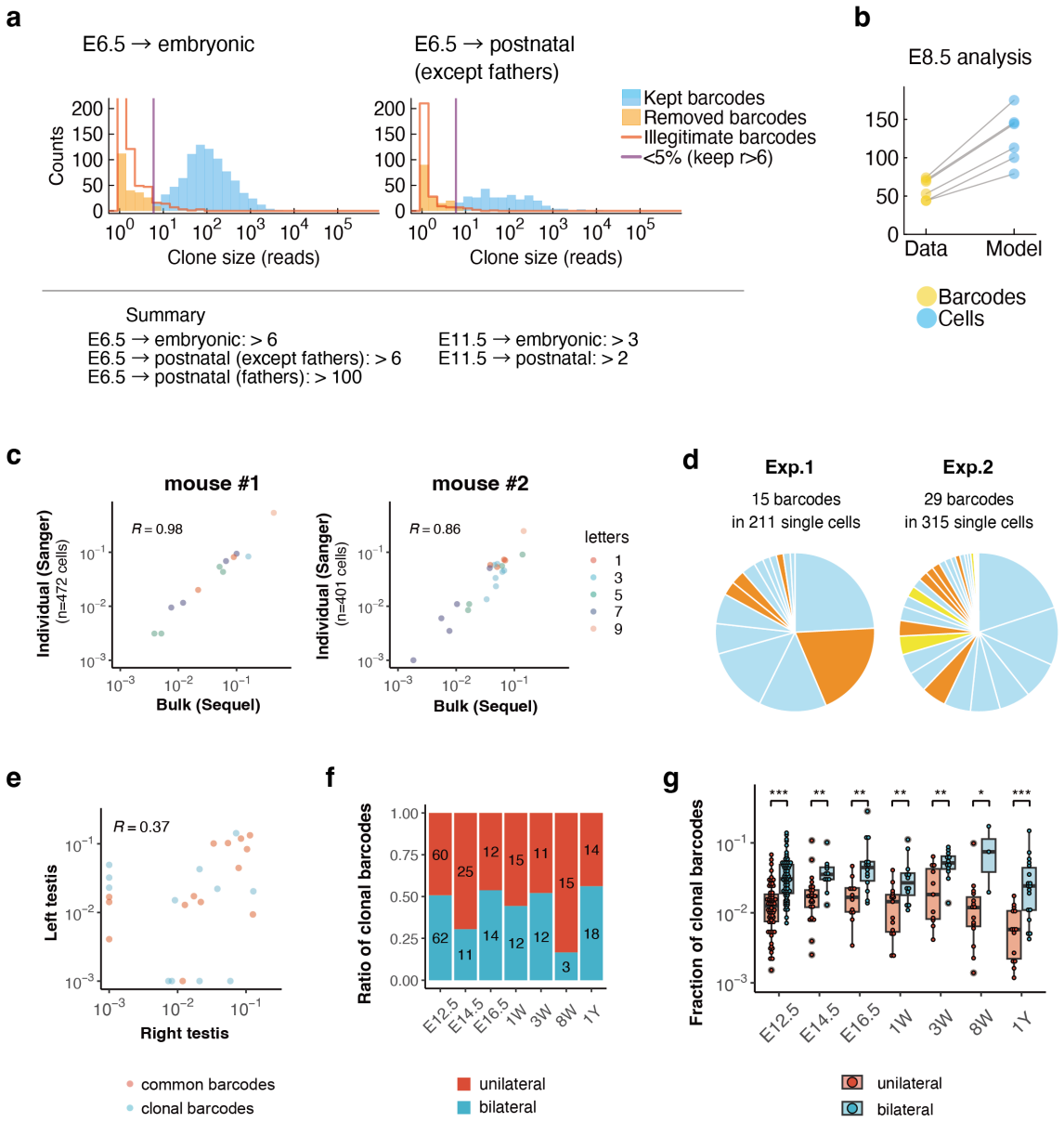

Extended Data Figure 2. Barcode analysis of E6.5&6.75-labeled PGC clones

a, Clone size (sequence read) distributions and criteria for barcode filtering. Barcodes were kept only if their clone size exceeded a defined threshold. The threshold (purple line) was set as the smallest clone size for which the number of remaining illegitimate barcodes (red) fell below 5% of the number of remaining legitimate barcodes (blue). Legitimate barcodes with clone sizes smaller than or equal to the threshold were

excluded from subsequent analyses (orange).

b, Estimation of the cell number leading to the observed barcode outcomes, inferred from a model simulation with a given number of cells recombining their *Polylox* cassette intrinsically. The model was fitted to find the most probable cell number (blue) best explaining the unique barcodes observed in E8.5 PGCs, after induced at E6.5&6.75 (yellow).

c, Validation of proportionality between the bulk barcode reads by amplicon sequencing using long-read sequencers (Sequel, Pacific Biosciences) and the actual composition of barcoded cells. A $CDH1^{+}/CD9^{+}/KIT^{-}$undifferentiated spermatogonia fraction (i.e., SSCs) were FACS-sorted from bilateral testes of two male mice, each barcoded at E6.5&6.75 and collected at 26 and 37 weeks of ages. On one hand, the *Polylox* sequences contained in this fraction were read by a bulk amplicon sequencing using Sequel; in parallel the same cell fraction was further sorted into individual cells, whose barcodes were amplified and read by Sanger sequencing. As displayed, the results of bulk sequencing showed strong linear correlation with individual read, irrespective of the letter length as colour-indexed. 10^{-3} was added to each barcode's frequency for $\log_{10}$ transformation; Spearman's rank correlation coefficients (R) are shown.

d, Composition of barcodes induced at E6.5&6.75 and analysed in E13.5 testes, through Sanger-sequencing the individually sorted PGCs. Results from two independent experiments were shown, with clonal barcodes indicated (P_{gen}<0.001 and <0.0011, orange and yellow respectively). These results consolidate the conclusion based on the bulk sequencing that single PGC-derived clones induced at E6.5 unequally expand during their migratory stage.

e, Barcode composition included in right and left testes, with common (P_{gen}≥0.001) and

clonal (P_{gen}<0.001) barcodes coloured in red and cyan, respectively. Representative results from a single mouse (ID: m060) were shown. 10^{-3} was added to each barcode frequency for $\log_{10}$ transformation; Spearman's rank correlation coefficient (R) is shown.

f, Fractions of clonal barcodes observed unilaterally versus bilaterally, collected from all mice harvested after E12.5.

g, Contributions of unilaterally versus bilaterally detected clonal barcodes in all recombined barcode reads. Note that bilaterally observed barcodes show significantly higher contributions at all time points. ***p<0.001, **p<0.01, *p<0.05, MWW.

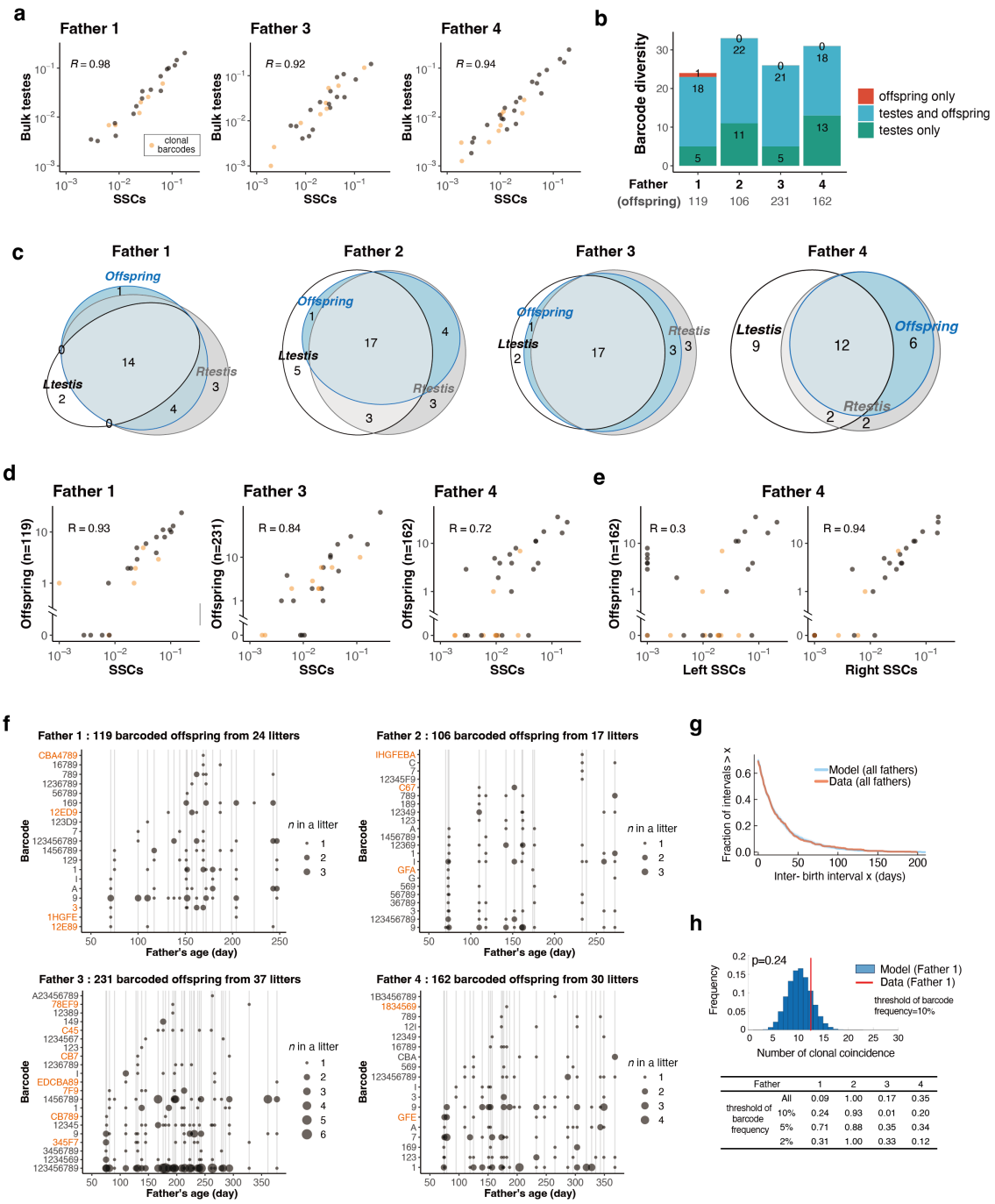

Extended Data Figure 3. Barcode transmission from SSCs through spermatogenesis to the offspring

Extended data for Fig. 2, involving four male mice barcoded at E6.5&6.75, mated with

multiple females, and had their testes sampled at 1 year of age; followed by barcode reading in their SSCs, bulk testes, and offspring.

a, Correlation between the barcode compositions in the SSCs and that in the bulk testes for three fathers but Father 2 presented in Fig. 2b. Note the similarly strong linear correlations. 10^{-3} was added to each barcode frequency for $\log_{10}$ transformation; Spearman's rank correlation coefficient (R) is shown.

b, A bar plot showing diversity of barcodes appeared in fathers' testes only (green), both father's testes and offspring (cyan), and offspring only (red), summarized for each of the four fathers. All but 1 barcode identified in offspring were also found in the testes. The exceptional one likely derived from a PGC clone that became extinct before Father 1 reached one year of age. The number of offspring carrying barcodes are indicated below.

c, Venn diagrams indicating barcode overlapping among the left testis (white), right testis (grey) and offspring (cyan), summarized for each father. Note that all barcodes that appeared in Father 4's offspring were included in Father 4's right testis.

d, Correlation between barcode composition in SSCs and in offspring, with the result from Father 2 shown in Fig. 2c. Note the similarly strong linear correlations. 10^{-3} was added to each barcode frequency for $\log_{10}$ transformation; Spearman's rank correlation coefficient (R) is shown.

e, Correlation between barcodes found in SSCs from left or right testis of Father 4 and those observed in its offspring. Note that barcodes in offspring show strong correlation with SSCs from the right, but not the left, testis, suggesting that offspring of Father 4 were derived exclusively from the right testis.

f, Summary of the barcodes transmitted to offspring, plotted for the father's age on

offspring's birthday. Grey vertical lines mark each litter's birthday; dots represent littermates whose size indicates the number of littermates sharing the same barcode. Clonal barcodes are coloured in orange.

g, Analysis of inter-birth intervals in reference to a random-shuffle model. Inter-birth intervals were aggregated from each father, quantifying the time between births of pups with the same barcode. Interval times of zero arise from barcode coincidences in pups of the same litter. Model simulations were obtained by shuffling the barcodes of all pups for each father randomly, and aggregating intervals as done for the data. Solid lines represent data (red) and the median of repeated model simulations (blue); band indicates 95% credibility region of the model.

h, Probability of clonal coincidence, defined as offspring sharing the same barcodes in the same litter, were compared between model and data. The representative plot (top) shows the result using barcodes of Father 1 with frequency lower than 10%. Blue columns indicate the probabilities of the number of the clonal coincidence calculated by Monte Carlo samplings. Red lines indicate the actual number of clonal coincidences observed in the experiments. Probabilities based on different thresholds of barcode frequency are also shown (bottom table). These tests hardly showed statistical significance, consistent with the idea that each offspring was derived from PGC clones randomly selected from an SSC pool.

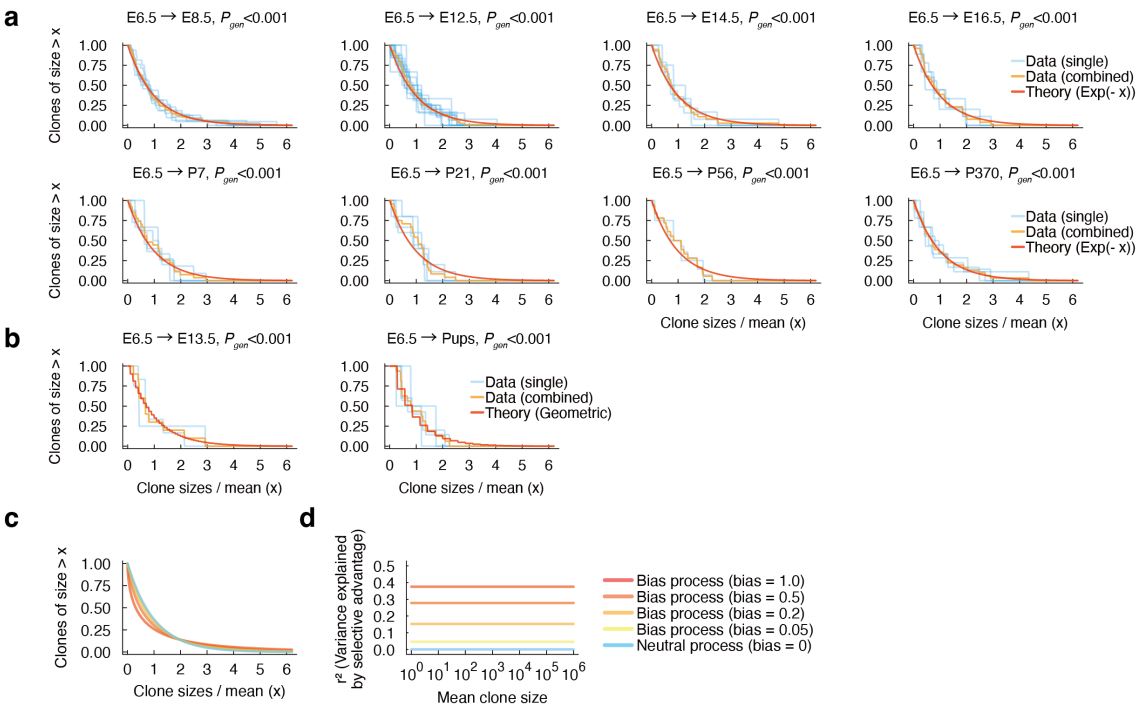

Extended Data Figure 4. Rescaled clone size distributions conforming with neutral birth-death processes

a, Size distributions of E6.5&6.75-barcoded PGC clones (i.e., read distribution of clonal barcodes with P_{gen}< 0.001) at indicated time points were rescaled by the mean value for each mouse (blue) and grouped mice (orange), and were compared to the theoretical distribution expected from a neutral birth-death process following the continuous scaling law of the exponential function (red; Supplementary Methods).

b, Size distribution of E6.5-induced PGC clones (with clonal barcodes) obtained from individual SSCs (analysed at E13.5) and from individual pups, compared to the theoretical distribution predicted by a discrete geometric model assuming neutral clonal competition.

c,**d**, Effect of clonal bias and persistent selective advantages on clone size distributions. Rescaled clone sizes (**c**) are compared between the neutral model (blue), assuming

neutral clonal competition without bias (birth-death models; **a**,**b**), with non-neutral dynamics at various bias levels (yellow to red). The bias parameter b is defined as $\mathrm{CV}_{\mathrm{bias}} = (1 + b)\ \mathrm{CV}_{\mathrm{neutral}}$, i.e. enhancing the coefficient of variation (CV) of the neutral clone sizes. Levels of clonal bias correspond to a certain fraction of the clone size variability that is explained by selective advantages between clones, as quantified by the squared correlation r^2 (**d**; Supplementary Methods). It holds that $r^2 = \big(b(b+2)\big)/\Big(2\big(1 + (b(b+2))\big)\Big)$, for any mean clone size. The remaining fraction of the clone size variability, $1 - r^2$, originates from neutral stochasticity. Clone size variability for $b = 0.2$ already deviates noticeably from the neutral case (**c**) and the data (**a**,**b**), indicating that PGC clone size variability is, by and large, driven by neutral stochastic effects (i.e., 85% - 100%).

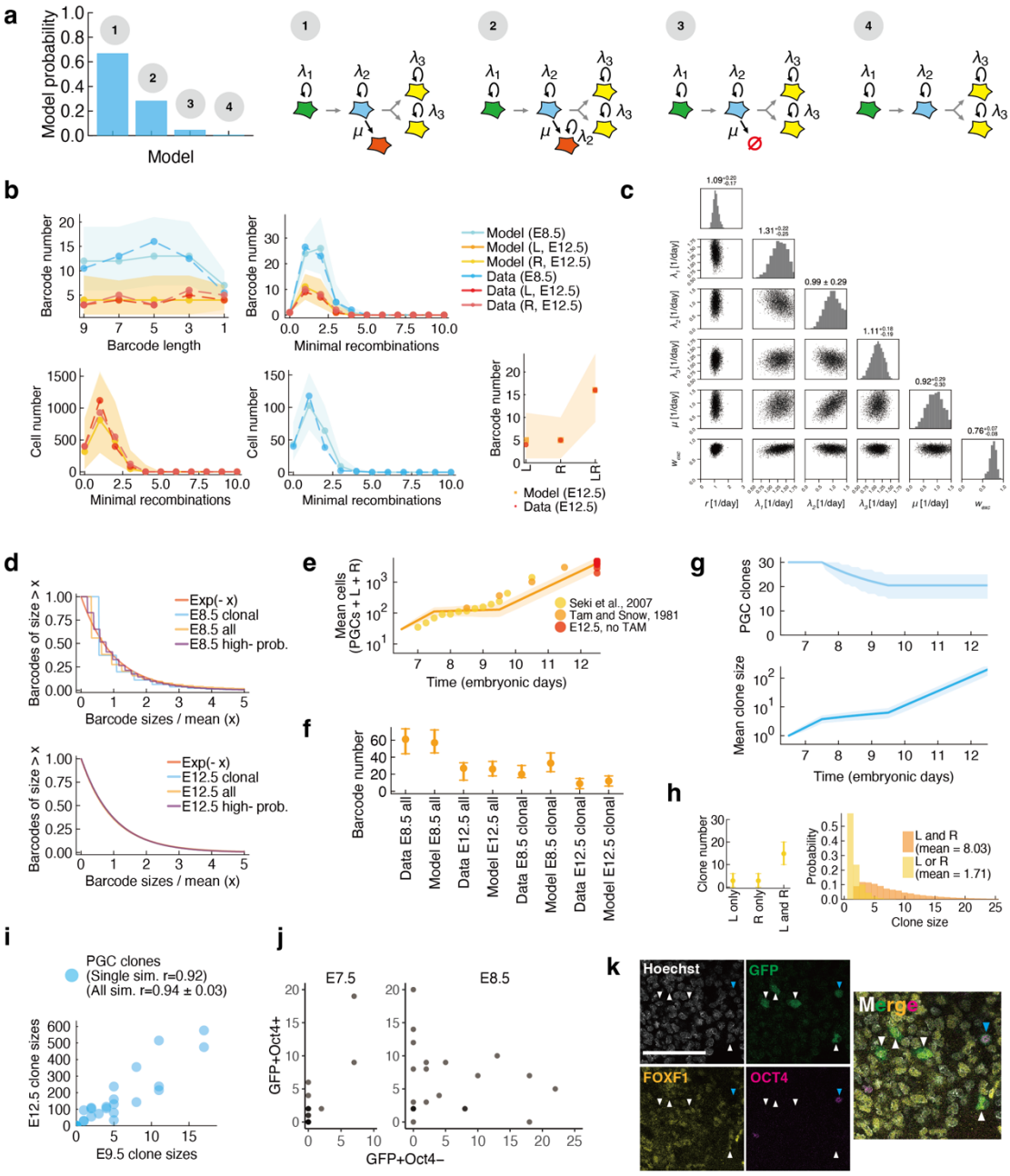

Extended Data Figure 5. Modelling the clonal dynamics of PGCs from E6.5 to E12.5

a, Posterior probabilities (left) inferred for the four tested modelling schemes (1-4; right). All models simulate PGC clonal dynamics in three sequential phases of birth-death processes from E6.5 to E7.5 (green), E7.5 to E9.5 (blue) and, after splitting into

left and right gonads, from E9.5 to E12.5 (yellow), following the respective division rates (λ_1, λ_2 and λ_3). The top model (1) simulates PGC loss with a rate μ from the second-phase PGCs (blue) into a non-arriving PGC fraction (red) that is still measured at E8.5 but does not proliferate and does not reach the gonads (yellow). Model 2 is like model 1, except that the non-arriving PGC fraction continues to divide with the same rate. Model 3 simulates PGC loss as immediate cell death. The model (4) which assumed all PGCs to survive without loss showed the lowest predictive capacity.

b, Barcode and clonal dynamics statistics used for the inference. Posterior statistics of the top model (Model 1 in (**a**)) are shown with 95% credibility bands, compared to the data as indicated.

c, Posterior parameter distributions as inferred from the data for the top model. The set contains biological parameters specifying PGC division and loss (λ_1, λ_2, λ_3 and μ), and technical parameters specifying the *Polylox* recombination kinetics (recombination rate r and excision bias w_{exc}).

d, Predicted distribution of *Polylox* barcode contribution simulated for E8.5 and E12.5 (top model with posterior parameters), rescaled with their means, based on clonal (blue), non-clonal/high-probability (purple) and all (orange) barcodes. In comparison, the theoretical scaling law of birth-death process (red) was indicated. The discreteness in E8.5 barcode sizes (upper panel) comes from the low cell numbers at this time point. Note the good agreement with the data, as shown in Extended Data Fig. 4 for clonal barcodes.

e, Predicted germ cell numbers (excluding non-arriving PGCs), shown as mean (lines) with 95% credibility bands. As reference, experimental measurements of embryonic PGC numbers are indicated (dot; see also Extended Data Fig. 1f).

f, Prediction of the total and clonal *Polylox* barcode numbers at E8.5 and E12.5 inferred by the top model, compared with the observed data. Median number (dot) with 5th and 95th percentiles (error bars) are shown. Note that the number of all barcodes is fitted in (**b**), but the clonal barcode numbers are a model prediction.

g, Prediction of the clone dynamics originated from E6.5 PGCs based on the top model with inferred parameters. Number of surviving E6.5 PGC-derived clones (top) and mean clone sizes of surviving E6.5 PGC-derived clones (bottom). Both model predictions (lines) are shown with 95% credibility bands.

h, Predicted number and size distribution of clones originating from the initial ~30 PGCs at E6.5, which arrived at the left (L) and/or right (R) gonads at E9.5, based on the top model with inferred parameters. Median clone number (dot) with 2.5^{th} and 97.5^{th} percentiles (error bars). The model predicts that left-right shared clones are bigger E9.5 and in the long terms, consistent with the experimental data (see also Fig. 3b, Extended Data Fig. 2g).

i, Correlation between the predicted clone sizes of the same clones between E9.5 and E12.5; a representative simulation (sim.) shown, correlation values indicated for the single and all simulations.

j, The numbers of $GFP^{+}OCT4^{+}$ and $GFP^{+}OCT4^{-}$ cells found in each of the E7.5 (left) and E8.5 (right) embryos.

k, Representative images of E8.5 allantois stained for GFP, OCT4, and FOXF. A significant portion of $GFP^{+}OCT4^{-}$ cells at E8.5 were positive for FOXF1, a marker of extraembryonic mesoderm including allantois[30] (white arrowheads). Scale bar, 100μm.

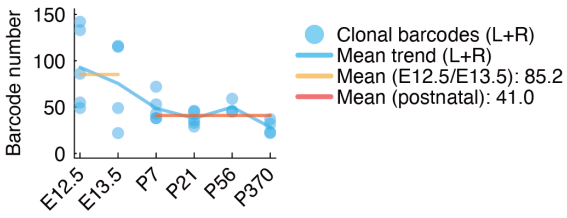

Extended Data Figure 6. Estimating the survival chance of single E11.5/E12.5 PGC-derived clones

Number of clonal barcodes (P_{gen}<0.00003; left and right testes combined) induced at E11.5 and recovered over embryonic and postnatal stages as indicated. The reduction in the mean number of clonal barcodes (horizontal lines) from ~85 in E12.5–13.5 to ~41 after birth indicates that the survival chance of a single PGC-derived clone from E12.5 to adult stages is approximately 50%. See Fig. 4b for total barcode numbers.

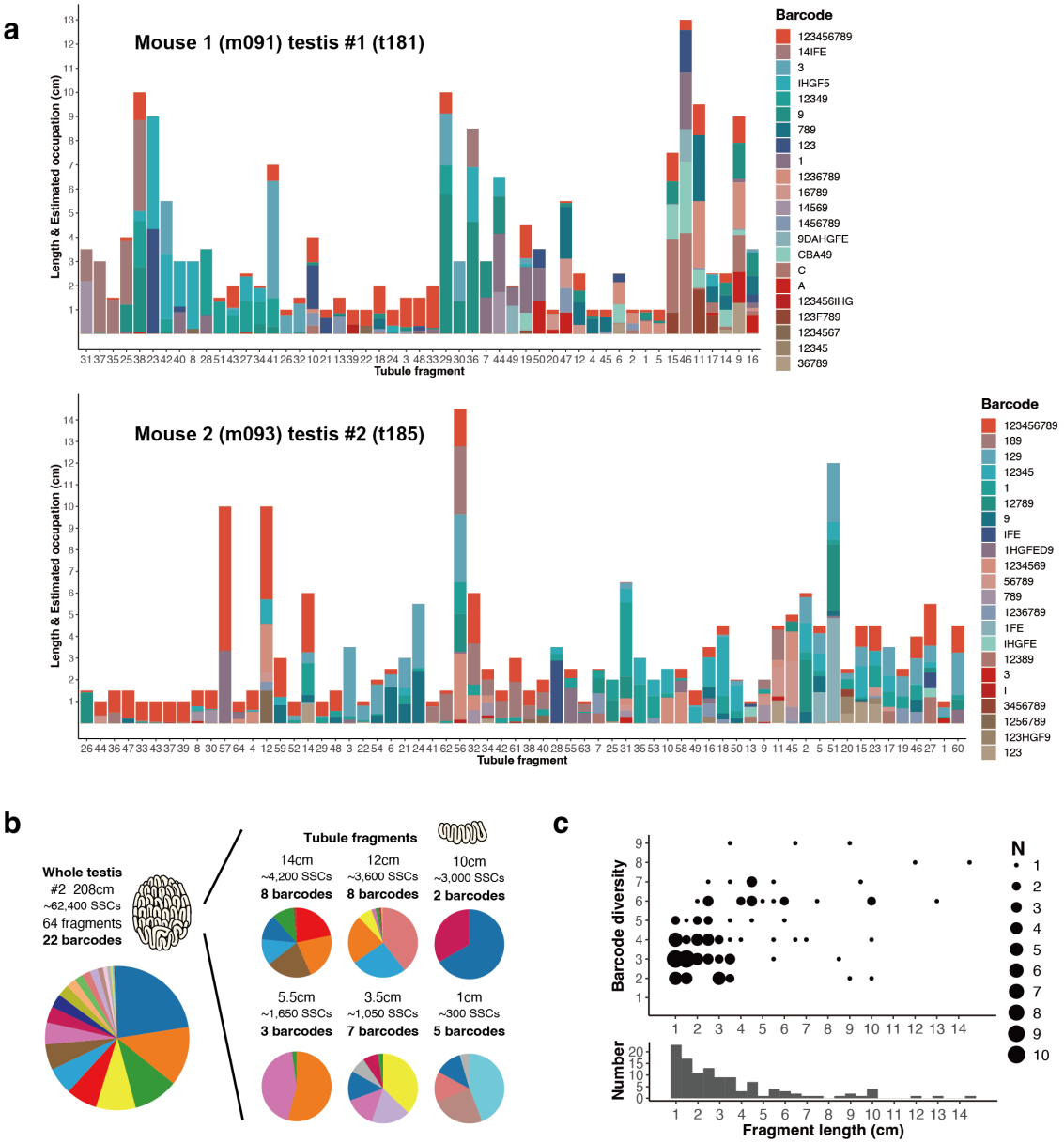
a
Mouse 1 (m091) testis #1 (t181)
Length & Estimated occupation (cm)
Tubule fragment
Barcode
123456789
14IFE
3
IHGF5
12349
9
789
123
1
1236789
16789
14569
1456789
9DAHGFE
CBA49
C
A
123456IHG
123F789
1234567
12345
36789
Mouse 2 (m093) testis #2 (t185)
Length & Estimated occupation (cm)
Tubule fragment
Barcode
123456789
189
129
12345
1
12789
9
IFE
1HGFED9
1234569
56789
789
1236789
1FE
IHGFE
12389
3
I
3456789
1256789
123HGF9
123
b
Whole testis
#2 208cm
~62,400 SSCs
64 fragments
22 barcodes
Tubule fragments
14cm
~4,200 SSCs
8 barcodes
12cm
~3,600 SSCs
8 barcodes
10cm
~3,000 SSCs
2 barcodes
5.5cm
~1,650 SSCs
3 barcodes
3.5cm
~1,050 SSCs
7 barcodes
1cm
~300 SSCs
5 barcodes
c
Barcode diversity
Number
Fragment length (cm)
N
d
Fragment_11
Fragment_29
Fragment_38
Fragment_46
Fragment_9
Fragment_15
Fragment_23
Fragment_36
Fragment_41
Length(cm)
Subfragment
Barcode

Extended Data Figure 7. Barcode distribution over the seminiferous tubules in the adult testis

a, Summary of two sets of barcode reads, each obtained from seminiferous tubule fragments representing a whole single testis each, separately sampled from two different individuals that were barcoded at E6.5&6.75 and sampled in 8 (Mouse 1) and 9 (Mouse 2) weeks of age. Each column represents the set of barcodes observed in a single fragment of the indicated length, colour-coded according to the identity and composition of barcodes, as specified on the right. Fragments are aligned on the x-axis according to hierarchical clustering of barcode frequency.

b, Summary of the uneven barcode distribution of the testis #2 from Mouse 2, presented in a same manner with Fig. 4d,e.

c, Number of barcodes found in each fragment with different lengths shown in the bottom. Data from the two testes (#1 and #2) are merged.

d, Barcode compositions in long contigs of tubule fragments obtained from testis #1 of Mouse 1, analysed separately in their subfragments. Subfragments are numbered in spatial sequence, except for the branched fragment (#46). Each column depicts each subfragment, with the total heights reflecting the tubule lengths and colours indicating the barcode identities (specified for each panel).

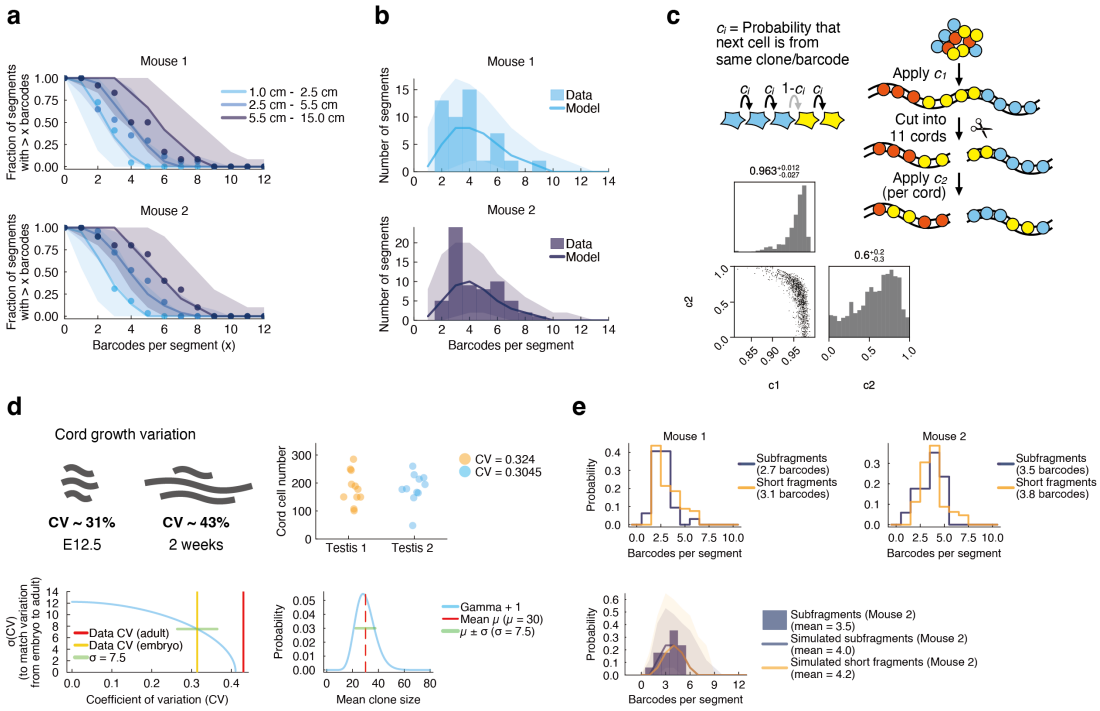

Extended Data Figure 8. Inference of a model for tubular PGC dynamics

Setup and inference of a model extending the PGC clone dynamics after E9.5, including phases of testis cord formation at ~E12.5, their expansion (E12.5 to 2 weeks), followed by homeostasis as analysed experimentally at 8 weeks.

a, Statistics used for the model inference. Distributions of *Polylox* barcode number included in tubule segments (Extended Data Fig. 7) were fitted simultaneously for three categories based on the indicated segment lengths for each of the two testes from two mice analysed (barcoded at E6.5&E6.75, simulated until 8 weeks after birth). Data (dots) and posterior model inference (solid lines with 95% credibility bands) shown.

b, Predictive capacity of the model validated in term of the distribution of barcode numbers across all analysed segments (data not directly used for fitting). Data (histograms) and the model prediction (solid line with 95% credibility bands) are overlayed.

c, Model setting of distributing the PGC clones upon compartmentalisation through testis cord formation at E12.5. The parameters c_1 and c_2 model the spatial distribution of clones on the forming ~11 tubule loops (effectively one-dimensional) at E12.5. Both parameters measure how strongly cells of the same clone form local clusters (top schemes). The first parameter c_1 controls the cluster sizes of clones within a cord at the time of compartmentalisation, and with that, the number of clones per cord. When PGCs subsequently align into the one-dimensional tubular arrangement, clusters may mix and yield the final organisation of local patches. The sizes of these local patches are controlled by the second parameter c_2 acting on the cluster sizes. Inferred posterior model parameters c_1 and c_2 (lower left).

d, Prediction of the variation in the extension of testis cords/seminiferous tubules within a single testis between E12.5 and 2W after birth. Summary of the coefficient of variation (CV) of cord cell numbers at E12.5 and in 2W after birth (top left), based on our measurement (see the top right panel) and Nakata et al., 2015[37], respectively. Numbers of germ cells included in individual testis cords of two E13.5 testes, with respective CVs indicated (top right). Shown values were rescaled to match the total germ cell number at E12.5 (~2,000) using E13.5 data (Extended Data Fig. 1f,g**)** as a close approximation. Inferring the cord variation parameter σ (i.e., the variability of extension of individual testis cords/seminiferous tubules within a single testis between E12.5 to 2W; bottom left). The blue line indicates the required heterogeneity to increase the initial embryonic CV to the adult CV during expansion. Best prediction of the 2W value from of the E12.5 value is given with $\sigma \approx 7.5$. (see Supplementary Methods). A gamma distribution was employed to simulate cord growth with the inferred cord variation parameter of $\sigma \approx 7.5$ (Bottom right).

e, Validation of our modelling scheme of heterogeneous extension of testis cords/seminiferous tubules (with $\sigma \approx 7.5$) by independent, barcodes-based data. Heterogeneous cord expansion (as specified by CVs in (**d**)) predicts a shift in the mean barcode number between short fragments and sub-fragments (pieces of a long fragment) when accounting for an identical underlying fragment length distribution. Data (top panels; means indicated in legend) show a slight shift of ~0.3 barcodes, consistent with the model prediction (lower panel) by ~0.2 barcodes (see Supplementary Methods for more details).

a

mouse_ID	day_old	Ltestis_color	Rtestis_color
1-1m	29	-	Y
1-2m	31	-	-
1-3m	31	-	-
2-1m	30	Y	RY
2-2m	35	-	Y
2-3m	35	RY	RY
3-2m	30	-	Y
3-3m	36	-	-
3-4m	36	-	-

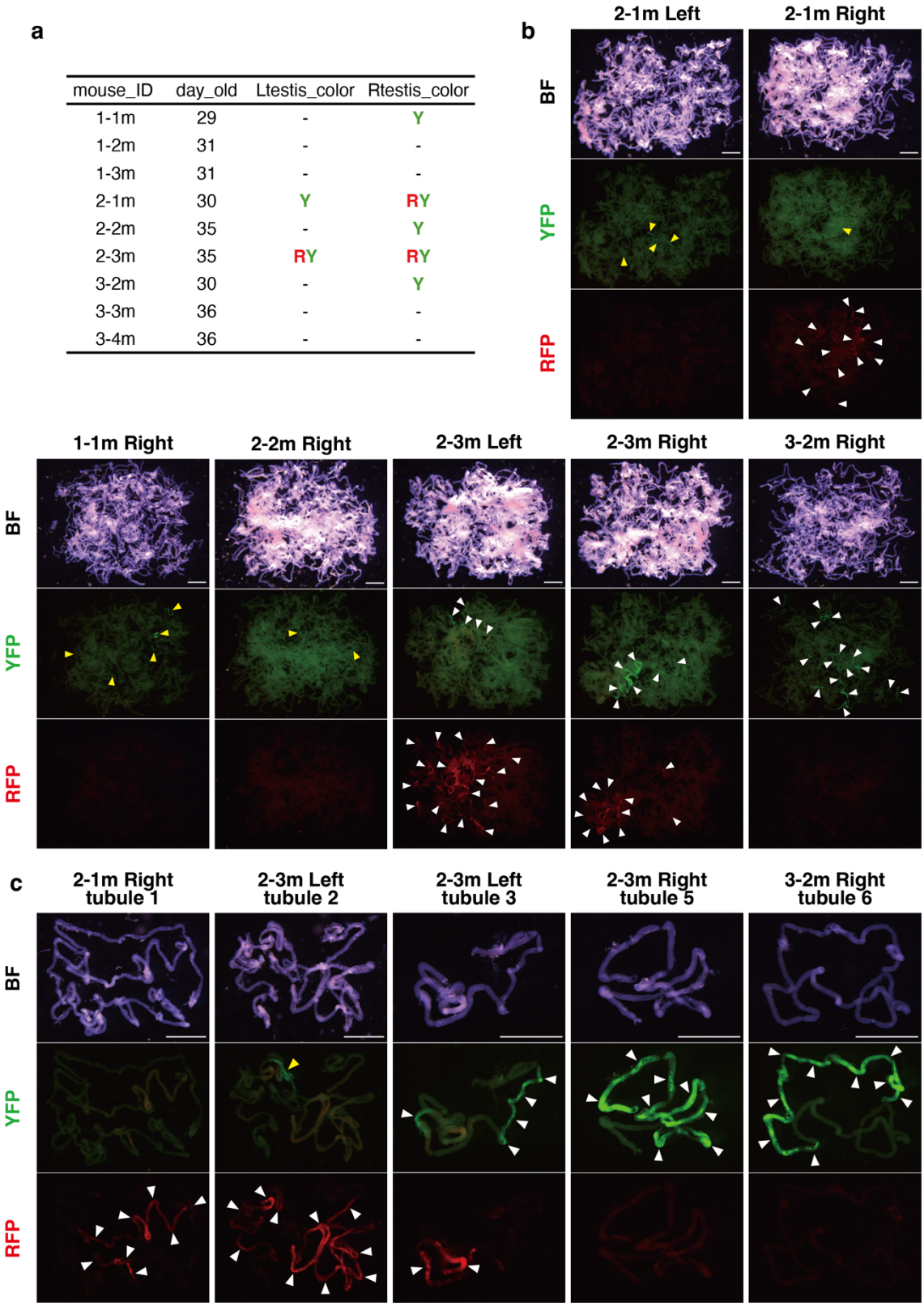

Extended Data Figure 9. Visualization of E6.5&6.75 PGC-derived clones in adult

using *Confetti* reporter, related to Fig. 5c

Following the experimental design presented in Fig. 5c top panel, PGCs were sparsely labelled at E6.5&6.75 and their clones were visualized at 4-5W after birth.

a, Summary of the analysed nine *Prdm14-MiCM*;*Confetti* mice and their fluorescent cells in their testes. R and Y indicate cRFP and cYFP, respectively. Note that only 5 in 9 mice contained fluorescent cells, and 4 of them having colours found only in unilateral testis, suggesting highly oligo-clonal labelling. mCFP and nGFP patches were not observed.

b, Thoroughly disentangled whole seminiferous tubules in testes of *Prdm14-MiCM*;*Confetti* mice. Seven testes in (**a**), which included one or more fluorescent-labelled patches are shown. Note the prominent green patches in 2-3m Left, 2-3m Right, and 3-2m Right, and red patches in 2-1m Right, 2-3m Left, and 2-3m Right testes (white arrowheads). Small green patches are also found, obscured by background signals in 1-1m, 2-1m and 2-2m (yellow arrowheads).

c, Higher magnification views of isolated fragments of seminiferous tubules carrying patches of fluorescence-labelled cells prepared from the indicated testes. Note prominent and extended green and red patches in tubules 3, 5, 6 and tubules 1, 2, 3, respectively (white arrowheads), and small green patches in tubules 2 (yellow arrowhead). Scale bar, 2mm.

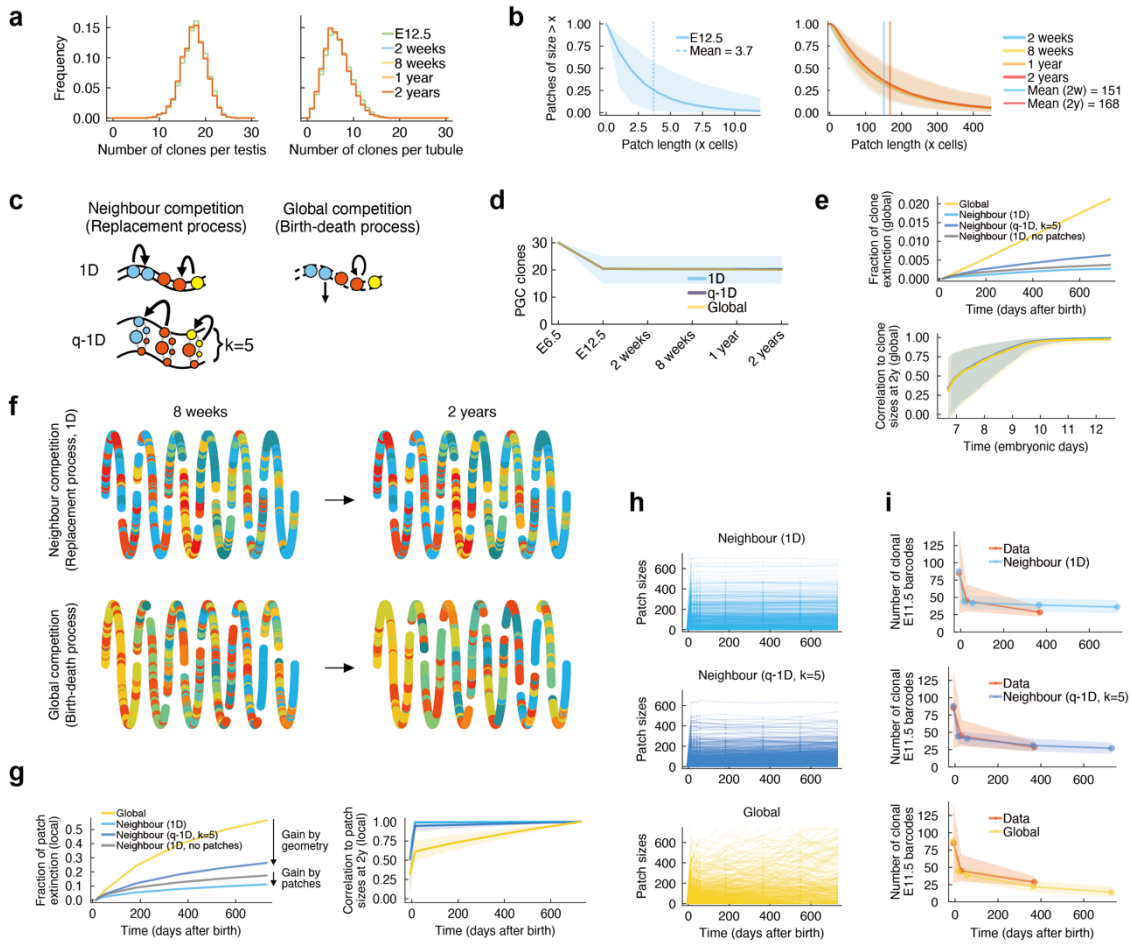

Extended Data Figure 10. Inferred spatiotemporal dynamics of PGC clones over the male lifespan

Lifelong dynamics of male germline clones (instead of *Polylox* barcodes) from their emergence at E6.5 to 2 years of age were inferred both globally (averaged over an entire testis) and locally (considering spatial organisation within seminiferous tubules). The integrative model consists of a sequence encompassing early clonal dynamics from E6.5 to E12.5, the formation and elongation of testis cords/seminiferous tubules by 2 weeks after birth, and an extended homeostatic phase lasting up to 2 years of age.

a, Model prediction for the number of surviving PGC clones within one testis (left) and

within one of the ~11 testis cords/seminiferous tubules (right), at different time points.

b, Model prediction of patch size distributions at E12.5 (left) and at multiple postnatal time points (right). Median prediction (solid lines) and 95% credibility band are shown, with mean patch sizes indicated by vertical lines. Homeostatic phase was modelled under neighbour competition dynamic within one-dimensional tubules.

c, Schemes of regulation modes during the adult homeostatic phase. Neighbour competition in tubules is compared to a hypothetical global competition model as reference, to investigate the effect of the tubular geometry on clone and patch size dynamics. In the scheme of neighbour competition (left), a lost stem cell through differentiation is replaced by one of the neighbours to maintain a constant stem cell pool. A one-dimensional (1D) geometry (left top), in which a lost stem cell is replenished by duplication of either the left or right neighbour. A quasi-one-dimensional (q-1D) tubular configuration (left bottom) with k=5 cells in the circumference (based on Klein et al., 2010[36]), in which a lost stem cells is replenished by duplication of any one of the 4 neighbours (left, right, bottom or top). In the hypothetical global competition mode (right; modelled as a critical birth-death process), stem cell loss and duplication occur stochastically and without spatial coupling, while maintaining a balanced total number of SSCs.

d, Model prediction for the number of surviving E6.5 PGCs (starting from ~30) up to 2 years (solid lines; 95% credibility band for 1D). Note that after E12.5, global PGC clones become very stable, in line with the observed *Polylox* barcodes induced at E6.5 (Fig. 1). Clone stability across the testis is robust, independent of the mode of adult homeostatic regulation (shown in (**c**)). Detailed dynamics for the early phase (E6.5 to E12.5) are shown in Extended Data Fig. 5g.

e, Model prediction for extinction probabilities and size correlation of global PGC clones following different modes of homeostatic regulation shown in (**c**). Over the testis wide, PGC clones show high stability from as early as ~E11, as indexed by low extinction during postnatal phase (top) and high correlation to their long-term clone sizes at 2 years (bottom), with the neighbour competition modes showing higher stability. Model bands show 95% credibility regions.

f, Model prediction of the spatial organisation of PGC clones in postnatal seminiferous tubules of a single testis from 8 weeks to 2 years of age, under different homeostatic regulation either by neighbour competition within tubules (upper panels) or by a hypothetical global competition as a reference (lower panels). In both scenarios, the testis is modelled as comprising 11 separate tubule loops, which contain a one-dimensional array of ~60,000 SSCs in total colour-coded by PGC clone identity (one of the ~30 initial clones). Cells belonging to the same clone (indicated by the same colour) often appear repeatedly as separate patches, within and across the tubule loops. Note the spatial organisation of such patches is high stable under neighbour competition, but unstable under a global competition.

g, Model prediction for extinction probabilities and size correlation of local patches, following different modes of homeostatic regulation shown in (**c**). The high stability of the neighbour competition dynamics is more clearly underscored by the fates of local patches, as evidenced by the extinction rates (left) and correlations with long-term patch sizes (right). Model bands show 95% credibility regions.

h, Model simulations of individual patch sizes over a testis, comparing different modes of homeostatic regulation. Note that global competition (birth-death process) shows lower stabilities as well.

i, Projection of the model dynamics by following the E12.5 germ cell-derived clones for their survival over time (compared for the three homeostatic regulation modes) with those observed in the E11.5 barcoding data (clonal barcodes, P_{gen}<0.00003). The q-1D setup in the neighbouring competition yielded the highest predictive power, likely due to the markedly smaller size of E12.5 germ cell-derived clones compared to those from E6.5 PGCs. Data and model bands show 95% credibility.

Supplementary Information

The methods and theory for modelling germline clonal dynamics are detailed in the following sections *1. Supplementary Methods* and *2. Supplementary Equations*.

1. Supplementary Methods

Scaling of clone size distributions. We assessed whether clone sizes from E6.5&6.75 PGC barcoding conform with the class of neutral birth-death processes; the theoretical basis for this procedure is given in Supplementary Equations a. We first applied the read threshold to filter spurious barcodes and subtracted the threshold from the kept clone sizes, so that the smallest possible clone size is again at one read (this mitigates censoring effects). Afterwards extant clone sizes were rescaled (divided) by their mean clone size, and the complementary cumulative probability distribution of the rescaled clone sizes was compared to the theoretical scaling law (Extended Data Fig. 4a,b). Further, this scaling of neutral clonal competition was compared to processes with inherent and persistent clonal biases (i.e., selective advantages) among the PGC clones at E6.5, confirming neutral stochasticity as the principal source underlying the observed clone size variation (Extended Data Fig. 4c,d; Supplementary Equations b).

Mechanics of *Polylox* recombination. *Polylox* barcode recombination was modelled as a Markov jump process in continuous time, each cell being subjected to a recombination rate r. We assumed this rate is the same for all cells during the entire recombination window; particularly, independent of the current barcode state. *Polylox* recombination was then simulated stochastically by starting all cells with the unrecombined barcode '123456789', selecting the next cell and time to recombine, conducting a recombination

888 (that is, changing the cell's barcode state) and continuing this procedure until the end of
889 the recombination window. The new barcode state was sampled from a
890 1,866,890×1,866,890 transition matrix specifying all legitimate *Polylox* recombinations[1].
891 Matrix values were assumed to be uniform, apart from a bias $w_{\mathrm{exc}} \in (0, 1)$ that tunes
892 chances of excisions vs. inversions. For example, barcode '123456789' has 45 possible
893 recombinations, 25 inversions (preserving barcode length 9) with probabilities
894 $c\,(1 - w_{\mathrm{exc}})$ each and 20 excisions (leading to lengths 7, 5, 3 or 1) with probabilities
895 $c\,w_{\mathrm{exc}}$ each, and $c = 1/(25\,(1 - w_{\mathrm{exc}}) + 20\,w_{\mathrm{exc}})$. Where applicable, such barcode
896 recombination was tied to other reactions of cellular dynamics (cell division, loss, etc.) in
897 a single model (see subsequent sections). At divisions, both daughter cells inherited the
898 barcode of the mother.
899
900 **Modelling PGC dynamics from E6.5 to E12.5.** To infer the lifetime clonal dynamics of
901 the ~30 PGCs induced at E6.5, we set up model inferences drawing from multiple
902 barcoding experiments, starting with analysis stages E8.5 and E12.5. We reasoned that
903 the accurate evolution of clonal loss and clone sizes are revealed from such a time-series
904 inference, in contrast to single snapshots alone. Further, we designed the approach to be
905 capable to switch between *Polylox* barcodes (introduced in a more continuous time
906 window from E6.5 to ~E8.0) and clones derived from single E6.5 PGCs.
907 First, we created four models of clonal PGC dynamics spanning from E6.5 to
908 E12.5 as continuous time Markov jump process with sequential phases of neutral birth-
909 death processes (as tested in section 'Scaling of clone size distributions'). All models
910 were initialized with thirty PGC clones at E6.5 that proliferated as a pure birth process
911 with division rate λ_1 until E7.5, and continued to divide during a subsequent migration

912 phase with rate λ_2 until E9.5. At E9.5 cells were randomly distributed to two
913 compartments, representing left and right gonads (later testes), where they proliferated
914 with rates λ_3 until E12.5. The models differ in their potential PGC loss during the
915 migration phase (Extended Data Fig. 5a). In model 1, PGCs were lost with a rate μ to a
916 non-arriving PGC fraction that was not distributed to the gonads at E9.5.

917 Second, we added *Polylox* barcodes to these models. Each cell was equipped with
918 an internal barcode state, starting with the unrecombined barcode '123456789' in all cells
919 at E6.5. Alongside the cellular dynamics, cells internally recombined their *Polylox*
920 barcode with a rate r and excision bias w_{exc} from E6.5 to E8.0 (see section 'Mechanics
921 of *Polylox* recombination'); after E8.0, barcodes were considered stable. Hence, given
922 values for its biological parameters (λ_1, λ_2, λ_3 and μ), each model simulated specific
923 E6.5 PGC dynamics. And, given additional values for the recombination parameters (r
924 and w_{exc}), these PGC dynamics were simultaneously probed with *Polylox* barcodes,
925 keeping track of barcode identities for all cells during the simulation.

926 These models were applied to *Polylox* barcoding data, using Bayesian parameter
927 inference and model selection from ABCdeZ.jl. We compared data and models via
928 summary statistics, iterating over many different parameter combinations. Flat priors
929 were chosen: pure birth rates λ_1 and λ_3 uniform in $[0.5, 1.75]$ (per day), the migration
930 parameters λ_2 and μ uniform in $[0, 1.5]$ (per day), the recombination rate r uniform in
931 $[0, 3]$ (per day) and the excision bias w_{exc} uniform in $(0, 1)$. Summary statistics for the
932 data were computed as median over all 6 and 13 mice for E8.5 and E12.5 analyses,
933 respectively. A first set of summary statistics informed about clonal diversity, using
934 distributions of *Polylox* barcode number (all barcodes used, no P_{gen} cutoff) over barcode
935 lengths (9, 7, 5, 3, 1) and minimal recombinations (0, 1, …, 11), and sharing of barcodes

936 between left and right gonads (E12.5 only). A second set of summary statistics informed
937 about total PGC cell numbers[23,24], using read distributions over barcode lengths and
938 minimal recombinations rescaled to 200 (E8.5) and 2000 cells (E12.5 for left and right
939 each). For each parameter set, models were simulated once until E8.5 and once until
940 E12.5, producing analogue model summary statistics from simulated *Polylox* barcodes.
941 The arriving and non-arriving PGC fractions were merged for the E8.5 readout if
942 applicable (models 1 and 2). After fitting each model to the data, posterior model
943 probabilities were obtained, and within each model, posterior parameter distributions.
944 To extrapolate to the clonal dynamics of the initial ~30 PGCs, the top model
945 (model 1) was re-simulated with median values of the biological parameter posteriors,
946 keeping track of the founding E6.5 PGC clones (instead of *Polylox* barcodes) for all cells
947 during the simulation.
948
949 **Clone initiating cell numbers for E8.5 analysis.** We fitted a recombination-only model
950 to observed barcode numbers of E8.5 analysis after E6.5&6.75 PGC barcoding, to assess
951 whether inferred cell numbers conform with the PGC numbers in the recombination
952 window (E6.5 to ~E8.0). The barcode data of each of the six mice (E8.5 analysis) was
953 transformed to summary statistics of absolute barcode number distributions over *Polylox*
954 barcode length (9, 7, 5, 3, 1) and minimal recombination number (0, 1, …, 10). For each
955 mouse, the recombination model was fitted to these data, producing the respective
956 summary statistics from simulations of *Polylox* barcode recombination in N cells at a
957 recombination rate r. Prior distributions were uniform on intervals $N \in \{1, \dots, 500\}$ and
958 $r \in [0, 4]$ (per day); the recombination window was fixed to 1.5 days and excision bias
959 to 75% (as inferred value of PGC E6.5 to E12.5 dynamics). The median of the posterior

960 distribution for N was reported as most likely cell number.

961

962 **Spatial and lifetime model of PGC clonal dynamics.** We extended the clonal PGC
963 dynamics inferred during embryonic development (Fig. 3, section 'Modelling PGC
964 dynamics from E6.5 to E12.5') in two aspects. First, starting around E12.5, PGCs in the
965 gonads localise in cord structures that become the seminiferous tubules of the testes
966 (Extended Data Fig. 1g). We wondered how PGC clones participate in the different
967 tubules and how they are locally distributed inside the effectively one-dimensional
968 tubules. Second, we aimed to model the dynamics of PGC clones over murine lifetimes,
969 both globally and locally. Together, this extended model provides a quantitative view of
970 the spatial and lifetime dynamics of E6.5 PGC clones.

971 We continued with PGC clone sizes from the left gonad after the lateral split
972 E9.5 (symmetric to right gonad), as inferred from the embryonic model. Clones were
973 expanded again as a pure birth process to reach ~2000 cells total at E12.5. At E12.5 the
974 expanded clones were then distributed on a one-dimensional spatial lattice, representing
975 the later spatial organisation of postnatal tubules: We introduced two parameters c_1 and
976 c_2 that allow to describe various types of spatial organisation, based on a theory for patch
977 formation (Supplementary Equations c). In short, $c_i \in [0, 1]$ specify the probabilities that
978 the next cell seeded to the spatial lattice is from the same clone as the previous cell. Cells
979 were distributed on a single lattice according to c_1, the lattice split up into 11 different
980 cords, and, lastly, cells were distributed within each cord lattice according to c_2. Hence,
981 c_1 captures clonal aggregation effects in the gonads before cord formation, leading to
982 biased cord participation, while the product $c_1 c_2$ describes the local mixing within a cord
983 after cord compartmentalisation, specifying the patch structure as it develops towards

984 postnatal analysis. As corner cases, this procedure contains fully randomized spatial
985 arrangements ($c_1 = c_2 = 0$), as well as fully aggregated scenarios ($c_1 = c_2 = 1$) where
986 all clones are laid out one after the other.

987 The developmental expansion from E12.5 to 2 weeks postnatally was modelled
988 as an expanding birth-death process on the spatial tubule lattices. Single cells on the
989 lattice across all cords were expanded with a mean amplification of 30 (from ~2000 PGCs
990 to ~60,000 SSCs per testis[52]) and a single-cell survival chance of 50% (specified by E11.5
991 barcoding, Extended Data Fig. 6). We factored in the appropriate level of cord-to-cord
992 heterogeneity in this mean expansion (roughly ranging from 20 to 40, Supplementary
993 Equations d, Extended Data Fig. 8d,e). Daughter cells of expanded clones were seeded
994 as immediate neighbours, leading to elongated tubule lattices.

995 From 2 weeks onwards, clonal dynamics were modelled as a homeostatic process
996 using neighbour competition with an average stem cell replacement time of once every 6
997 days (following previous studies[36,54]). Concretely, whenever a stem cell differentiated, its
998 empty lattice position was immediately taken by a random left or right neighbour that
999 duplicated in the process. Furthermore, effects of different homeostatic regulations were
1000 analysed (see section 'Neighbour and global competition during adult homeostasis').

1001 By using E9.5 clone sizes from the embryonic phase inference and fixing many
1002 model parameters as specified above, c_1 and c_2 were the only remaining parameters to be
1003 inferred from data. Again, we resorted to simulation-based inference by ABCdeZ.jl. Data
1004 of *Polylox* tubule fragments (E6.5&6.75 barcoding, 8- or 9-weeks analysis) were
1005 converted to summary statistics of complementary cumulative probability distributions,
1006 specifying the fraction of segments exceeding a certain barcode number (for three
1007 different categories of segment lengths and two independent mice; Extended Data Fig.

1008 8a). Starting from flat uniform priors over $[0, 1]$ for c_1 and c_2, analogue model summary
1009 statistics were computed iteratively and compared to the data. For the inference, again
1010 *Polylox* barcodes were taken as clone sizes. To obtain model summaries, tubules were
1011 simulated until 8 weeks postnatally and then cut into fragments matching fragment
1012 lengths of the data (using a conversion of ~30 SSCs per mm tubule[52]). Fitting the model
1013 to the data yielded a correlated posterior distribution for c_1 and c_2.
1014 To gain the spatial and lifetime dynamics of E6.5 PGC clones, we extrapolated
1015 again to the initial ~30 E6.5 PGCs by re-simulating this extended model with c_1 and c_2
1016 samples from their two-dimensional posterior and keeping track of PGC clone identity
1017 (instead of *Polylox* barcodes). The model was evaluated at various embryonic and
1018 postnatal time points, and local patch sizes as well as global clone sizes (summing all
1019 patches of same PGC identity) were inspected.
1020
1021 **Neighbour and global competition during adult homeostasis.** We investigated the
1022 potential advantages of the specific geometry of seminiferous tubules for the lifetime
1023 stability of PGC clones. The standard neighbour competition was simulated in one- or
1024 quasi-one-dimensional (1D or q-1D) tubular geometries, and compared to a hypothetical
1025 reference model with global competition that is agnostic towards geometric
1026 dimensionality or form. Simulations showed that the tubular geometries provide superior
1027 stability in contrast to the non-geometric reference; a feature that is further supported by
1028 Supplementary Equations e.
1029 The spatial and lifetime PGC dynamics were re-simulated as before (see section
1030 above), until the postnatal homeostatic phase at 2 weeks was reached. From that point
1031 onwards, the tubules were simulated in three different ways (Extended Data Fig. 10c).

First, as a neighbour competition process on a 1D lattice where left and right neighbours may replace each other (as before, section 'Spatial and lifetime model of PGC clonal dynamics'). Second, as neighbour competition on a q-1D cylindrical lattice, where left/right and below/above neighbours may replace each other. The circumference contained 5 cells with periodic boundaries[36], and hence ~12,000 units in the longitudinal dimension for a total of ~60,000 cells. Third, a reference global competition process, modelled as a critical birth-death process where events of cell division and differentiation balance out on the population average. Clones in the birth-death process develop independently of their neighbours and were assumed to be non-mixing at patch boundaries. All three scenarios were simulated with a stem cell division rate $\lambda = 1/6$ (per day; as before), so that the production of differentiated progeny and sperm would be identical.

Simulations tracked E6.5 PGC clones for various time points across the three scenarios. Global clone sizes and local patch sizes were collected to compute end-point-correlations and extinction levels. To quantify the gain of patch stability coming from the inferred average patch size of ~150 cells (Extended Data Fig. 10b), a hypothetical no-patch case was computed by using the single-cell patch extinction probabilities of a 1D neighbour competition model (Extended Data Fig. 10e,g). The single-cell extinction is given by $p(\ell_t = 0) = 1 - e^{-2\lambda t}\big(I_0(2\lambda t) + I_1(2\lambda t)\big)$ (Supplementary Equations e), and hence the extinction chance for a "patch" of ℓ cells, being instead scattered on the lattice, was computed by $p(\ell_t = 0)^{\ell}$. Another set of simulations tracked single cells introduced at E12.5 in otherwise identical models, to compare clonal diversity over time with the E11.5 barcoding data (Extended Data Fig. 10i).

Temporal transmission bias from fathers to pups. We assessed whether PGC clones have a temporal bias in their contribution to pups over the father's life span. To that end, we computed the times between occurrences of the same barcode and aggregated these inter-birth intervals for all barcodes and the four fathers. A value of zero days corresponds to barcode coincidences in two or more pups on the same day. To obtain a model reference of unbiased barcode transmission, the barcodes were randomly shuffled across the pups of a given father and inter-birth intervals were recomputed as done for the data. The data distribution of inter-birth intervals was compared to the unbiased model based on repeated simulations providing median and 95% credible intervals (Extended Data Fig. 3g). Further, the data was reduced to barcodes with a maximum barcode frequency of 10%, 5% or 2% and simulations of the unbiased model were recomputed to obtain right-tailed *p*-values under a null distribution for clonal coincidences[55] (Extended Data Fig. 3h).

2. Supplementary Equations (a, b, c, d and e)

a, Rescaled clone size distributions of single PGCs. Analysis of rescaled clone size distributions (as done in Extended Data Fig. 4a,b) shows that clonal dynamics of PGCs conform with a neutral birth-death process. Due to this observation, we implemented the models for the barcoding data based on these stochastic processes (dynamics from E6.5 to E12.5, Fig. 3, and also extended from E6.5 to 2 weeks, Fig. 5). The clone sizes from E6.5 barcoding reveal the nature of the clonal dynamics in the expanding embryonic phase. The scaling law then applies even for adult analysis stages, as clones stabilise before entering the adult homeostatic phase (compare with Fig. 3) and continued turnover is neutral among surviving clones (see also Supplementary Equations b, Extended Data Fig. 4c,d). We briefly outline the well-known theory of birth-death processes, to state the

scaling law that we applied to the barcoding data.

In birth-death processes, two types of transitions are possible: An individual cell may divide with chance $\lambda(t)\mathrm{d}t$ ("birth") and leave the compartment of interest with chance $\mu(t)\mathrm{d}t$ ("death") in any short time span $\mathrm{d}t$. The division and loss rates, $\lambda(t)$ and $\mu(t)$, are the same for all cells in the considered compartment. Particularly, they are independent of the clone identity and current clone size, and as such the process is neutral. The rates may however vary as a function of time t; this includes our models with sequential phases. For this process, the probability distribution of clone sizes $X_t = x$ at time t for any initial clone size $X_0 = x_0$ are available (simple non-homogenous birth-death process; Bailey, 1964[56]). Focusing on clones derived from single cells, $x_0 = 1$, the distribution is given by $p(x) = (1-\alpha)\,(1-\beta)\,\beta^{x-1}$ (for $x \geq 1$) and $p(0) = \alpha$, where $\alpha = 1 - 1/\left(e^{\rho(t)} + A(t)\right)$ and $\beta = 1 - e^{\rho(t)}/\left(e^{\rho(t)} + A(t)\right)$ with $\rho(t) = \int_0^t \{\mu(\tau) - \lambda(\tau)\}\mathrm{d}\tau$ and $A(t) = \int_0^t \lambda(\tau) e^{\rho(\tau)}\mathrm{d}\tau$. The solution includes the time-homogenous processes (critical, sub- and supercritical). For *Polylox* data it is natural to condition this distribution on survival (as we can only observe extant clones that did not go extinct before analysis). Under this condition, $X_t \geq 1$, the distribution simplifies to a shifted Geometric distribution with $p(x) = (1-\beta)\,\beta^{x-1}$, where $x \in \{1, 2, \ldots\}$, and mean clone size $\mathbb{E}(X_t) = 1/(1-\beta)$. So, while considering a broad class of processes, all clone sizes fall on the same distributional shape with only one effective parameter—its mean clone size.

Thus, we rescale the extant clones with their mean. We consider $W_t = X_t/\mathbb{E}(X_t)$ and obtain $p(W_t > w) = \beta^{\lfloor w/(1-\beta)\rfloor}$, with floor function $\lfloor\,\rfloor$. Further, in the continuous limit for expanded clones ($\beta \to 1, w > 0$), rescaled clone sizes simplify to $p(W_t > w) = e^{-w}$. Both expressions were used (Extended Data Fig. 4a,b) and pose a

simple but strong test of neutrality and compatibility with the class of birth-death processes.

Of note, other neutral processes (e.g., homeostatic Moran process without selection) can settle on the same scaling law[57]. We further note that non-simultaneous introduction of clonal barcodes *in vivo* should not be a problem for the scaling analysis: Clonal barcodes in model simulations (being created over a 1.5-day recombination window) still scale (Extended Data Fig. 5d), showing that this effect does not distort clone sizes significantly in our system. Lastly, the random split of clone sizes (binomial sampling) into left and right gonad is allowed within the above birth-death processes. Binomial sampling is mathematically equivalent to a pure death process, and hence the stated distributions and scaling laws remain unchanged.

b, Theory of inherent and persistent clonal bias. In the following we derive a theory to investigate whether, and to which degree, clone sizes that conform with the neutral scaling law (Supplementary Equations a) actually indicate an underlying neutral mechanism. To that end, clonal dynamics are considered where some clones exhibit inherent and persistent selective advantages, termed "clonal bias", deviating from purely neutral behaviour. We find a criterion that directly links non-neutral clone sizes to the fractions of clone size variability that are caused by clonal bias and neutral stochasticity, respectively. This theory confirms that the principal source underlying the observed germline clone size variation is neutral stochasticity (85% - 100%).

Following up on Supplementary Equations a, we start by considering single-cell derived, extant clones driven by birth-death dynamics. Under neutral clonal behaviour, clone sizes $X = x$ at analysis follow the distribution $p(x) = (1 - \beta)\, \beta^{x-1}$,

$x \in \{1, 2, \dots\}$, where β, and hence the mean clone size $\mathbb{E}(X) = 1/(1-\beta)$, is identical for all clones. To introduce systematic clonal bias and selective advantages, we now lift this assumption and allow for clone-specific dynamics and mean sizes. Concretely, a random variable g, the clone-specific mean clone size, is introduced such that $\mathbb{E}(X \mid g) = 1/\big(1-\beta(g)\big) \equiv g$ for individual clones. This means that each individual clone evolves according to division and loss rates identical across all its constituent cells; however, these rates may vary across cells of different clones. To parametrize g on the mean and variance level, we set $\mathbb{E}(g) = \mu$ and $\mathrm{Var}(g) = \sigma^2$. The neutral case is then contained with $\sigma = 0$, while $\sigma > 0$ implies that some clones will obtain a selective advantage (for events $g > \mu$) and others are disadvantaged ($g < \mu$). The mean observed clone size across all (potentially biased) clones is calculated to $\mathbb{E}(X) = \mu$, independent of neutral or non-neutral dynamics. In contrast, the variance across all clones is given by $\mathrm{Var}(X) = (\mu-1)\mu + 2\sigma^2$ leading to a coefficient of variation (CV) of $\mathrm{CV}(X) = \sqrt{\mathrm{Var}(X)}/\mathbb{E}(X) = \sqrt{1 - 1/\mu + (2\sigma^2)/(\mu^2)}$. Here, while neutral dynamics approach a maximal CV of one, non-neutral dynamics can generate clone size variation beyond this limit.

To obtain a "scale-free" view on clone size variability, i.e. independent of the mean clone size μ, we introduce a dimensionless bias parameter b that quantifies the excess of non-neutral clone size variation beyond the neutral baseline. Concretely, we set $\mathrm{CV}(X) = (1+b)\sqrt{1-1/\mu}$, where $b \geq 0$ and $\sqrt{1-1/\mu}$ is the CV of the neutral case ($\sigma = 0$). From this, one obtains the conversion $\sigma = \sqrt{(1/2)\, b(b+2)\,(\mu-1)\mu}$. Such clonal bias, quantified via b, allows to directly compare the shapes of scale-free clone size distributions (i.e., rescaled) for neutral ($b = 0$) and various non-neutral clonal dynamics ($b > 0$), as done in Extended Data Fig. 4c ($b \in \{0.0, 0.05, 0.2, 0.5, 1.0\}$). To

visualize concrete distributions, g was sampled from a shifted gamma distribution, setting $g \sim \mathrm{Gamma}(\alpha, \theta) + 1$ (with shape α and scale θ) and $\alpha = ((\mu - 1)/\sigma)^2$ and $\theta = (\mu - 1)/\alpha$, where σ was specified by the above conversion from b and μ. Then $\mathbb{E}(g) = \mu$ and $\mathrm{Var}(g) = \sigma^2$ as desired.

It remains to be investigated to what extent inherent clonal bias (or selective advantages) actually causally contributes to the observed variation of clone sizes (the shapes of these rescaled distributions). For this, the observed extant clone sizes, X, are correlated with their inherently biased means, g. If initial biases among clones faithfully predict and determine later "winner" and "loser" clones (i.e., big and small clones), this equates to a high correlation. In contrast, a low correlation reveals that—even if biases among clones may exist—neutral stochasticity dominates effects of clonal bias so that the "winner" and "loser" clones are simply determined by chance. In this sense, the squared Pearson correlation $r^2(X, g)$ determines the fraction of the clone size variance that is explained by clonal bias ($\mathrm{Var}(X)$ explained by g) and is computed subsequently. First, the joint expectation can be derived to $\mathbb{E}(Xg) = \mathbb{E}(g^2) = \mu^2 + \sigma^2$. Then, it follows that $r^2 = \mathrm{cor}(X, g)^2 = \mathrm{Var}(g)/\mathrm{Var}(X) = \sigma^2/\big((\mu - 1)\mu + 2\sigma^2\big)$. Finally, by using the above conversion to express σ in terms of the clonal bias b and mean clone size μ, one obtains the result $r^2(X, g) = (1/2)\big(b(b + 2)\big)/\big(1 + b(b + 2)\big)$, which becomes independent of μ. Hence, shapes of the rescaled clone size distributions, as set by the clonal biases b, directly relate to the fraction of clone size variability, r^2, attributable to inherent and persistent selective advantages. The remaining fraction, $1 - r^2$, is hence the clone size variability explained by neutral stochasticity. This result provides a simple yet powerful criterion to assess the contributions of neutral vs. selective clonal dynamics directly from the observed variation of clone sizes.

Comparing the theoretical clone size distributions (Extended Data Fig. 4c) to the experimental distributions (Extended Data Fig. 4a,b) reveals no skewness in the data as it would be expected from inherent clonal bias. Additionally, already a bias of 20% ($b = 0.2$) deviates noticeably from the neutral distribution (Extended Data Fig. 4c), and, as such, may be considered the maximal clonal bias hidden in the data. This extent of clonal bias corresponds to a causal contribution of 15%, at maximum, to the observed clone size variability; conversely, at least, 85% of the variability is caused by neutral stochasticity (Extended Data Fig. 4d). Together, these results show that clonal dynamics that appear neutral also indicate an underlying neutral mechanism. The neutral clone sizes of the germline hence pose a strict restriction to the level of inherent and persistent selective advantages among PGC clones. If inherent clonal biases exist at all, they must be either rather transient or mild in effect.

c, Theory of patch formation. We derive a theory for the patches that a clone forms when being distributed on a one-dimensional spatial lattice, representing the forming cords in the embryo and the later tubules in postnatal testes. Patch formation is described by a local correlate of how much a clone identity of a cell predicts the clone identity of its neighbouring cells. Concretely, we introduce a probability $c \in [0, 1]$ that the next cell on the lattice, viewed from left to right, is occupied by a cell of the same clone. This principle, starting from a patch with its first cell, induces patch lengths (or sizes) $\ell \in \{1,2, \dots\}$ that follow a shifted geometric distribution ($\ell - 1$ "successes", i.e. further cells of the same clone, before the first "failure") with probabilities $p(\ell) = (1 - c)\, c^{\ell-1}$. However, for a clone of N cells total, a patch length has to be bounded by $\ell \leq N$, and the fragmentation of the clone leads to $n \in \{1, \dots, N\}$ distinct patches of sizes ℓ_i, such that

$\sum_{i=1}^{n} \ell_i = N$. Hence, we aim to derive, conditioned on the clone size N and c given, the distribution of the number of patches $p(n|N)$ and the distribution of patch lengths $p(\ell_i|n, N)$ for each patch i.

To compute $p(n|N)$ one notes that the inverted probability $p(N|n)$ is given by a shifted negative binomial distribution, as the sum of independently formed patches that are geometrically distributed with $p(\ell_i)$. We have $N|n \sim \mathrm{NegBin}(n, 1-c) + n$ with probabilities $p(N|n) = p(\sum_{i=1}^{n} \ell_i \,|n) = \binom{N-1}{n-1} c^{N-n} (1-c)^n$. Then Bayes theorem allows the conversion to $p(n|N)$. With an uninformed prior for the number of patches, $p(n) = 1/N$, one obtains $p(n|N) = \binom{N-1}{n-1} c^{N-n} (1-c)^{n-1}$. Thus, the number of patches follows a modified binomial distribution, $n|N \sim \mathrm{Bin}(N-1, 1-c) + 1$, with a mean patch number $\mathbb{E}(n|N) = (N-1)(1-c) + 1$, and noteworthy corner cases of a single patch containing all N cells at once ($n = 1$ if $c = 1$) vs. N single-cell patches ($n = N$ if $c = 0$).

Given c and clone size N, and with that also the patch number n from above, the distribution of patch sizes $p(\ell_i|n, N)$ is obtained in iterative manner. We introduce ℓ_1, the size of the first patch and, stochastically independent, $\ell_{-1} = \sum_{i=2}^{n} \ell_i$, the combined sizes of the patches after the first. It follows $p(\ell_1 = x|n, N) = p(\ell_1 = x)\, p(\ell_{-1} = N - x)/p(\ell_1 + \ell_{-1} = N)$ (where the right-hand side probabilities are shifted negative binomial distributions from above), leading to $p(\ell_1|n, N) = \binom{N-1-\ell_1}{n-2} / \binom{N-1}{n-1}$, with patch sizes in the range $1 \leq \ell_1 \leq N - n + 1$. Further, we derive that all subsequent patch sizes can be obtained iteratively: The patch size ℓ_i is given by the same distribution, only by updating $N_{new} = N - \ell_{i-1}$ and $n_{new} = n - 1$; for example, the second patch length is given by $p(\ell_2|\ell_1, n, N) = \binom{N-\ell_1-1-\ell_2}{n-3} / \binom{N-\ell_1-1}{n-2}$. We implemented an algorithm to robustly evaluate the involved ratio of binomial coefficients, termed the $\mathrm{BinRatio}(n, N)$

distribution in code. The mean value of this distribution is $\mathbb{E}(\ell|n, N) = N/n$, while the mean patch length over all (random) patch numbers n is computed to $\mathbb{E}(\ell|N) = (1 - c^N)/(1 - c)$.

Of note, this theory is closed under repeated patch formations: Fragmenting a clone of N cells with $c_1 \in [0,1]$ and fragmenting the resulting patches (viewing patch lengths as clone sizes ℓ_i) another time with $c_2 \in [0,1]$, is identical to a single fragmentation using the product value $c = c_1 c_2$ on the initial clone size N directly. This indicates that complex biological fragmentation processes may be well-captured descriptively by a single or few parameters, correlating clone identities of cell neighbours.

Combining above derivations, a list of patch sizes can be generated over all clones, by first sampling the number of patches for a given clone and then sampling the size of each patch iteratively. In summary, this theory provides a full stochastic framework to spatially distribute clones with given clone sizes on a one-dimensional lattice, encapsulated in a single parameter c that specifies the statistics of the number and lengths of the formed patches.

d, Theory of foetal patch elongation dynamics. We develop a model for the dynamics of patch sizes inside the expanding tubules, spanning from cord formation (E12.5) to the postnatal tubules (2 weeks) at which the homeostatic phase is entered. The model accounts for growth differences in the cords (that is, some cords elongate to long tubules in the adult, some to short), at a magnitude that we validate through independent features in the barcoding data.

Each gonad (the later testis) forms ~11 cords (the later tubules) that roughly expand from 2,000 PGCs at E12.5 to 60,000 SSCs at two weeks after birth (and thereafter),

meaning that PGCs amplify 30-fold on average. We compare the coefficient of variation (CV) at these two time points, to assess to what extend PGC expansion is heterogeneous across different cords. Embryonic cord cell numbers have a $\mathrm{CV}_{\mathrm{E12.5/E13.5}} \approx 0.31$ (Extended Data Fig. 1g and 8d), that increases to $\mathrm{CV}_{\mathrm{adult}} \approx 0.43$ (Nakata et al., 2015[37]; where tubule T6 was excluded as a likely merger two cords; Extended Data Fig. 8d). Subsequently a theory is derived to show that this increase in variation cannot be explained by homogenous stochasticity of PGC expansion but warrants systematic growth differences between elongating tubules.

We assume that a cord i has X_i cells initially (E12.5), elongating to Y_i cells postnatally. Within a given cord, single PGCs follow an expanding (supercritical) birth-death process, captured in the random variables Z_{ij}, such that the sum of all single PGC expansions generates the elongated tubule, i.e. we have $Y_i = \sum_{j=1}^{X_i} Z_{ij}$. We inform single-cell expansions by the mean $\mathbb{E}(Z_{ij}) = \mu = 30$ (from 2,000 to 60,000, over all cords), and survival chance $p(Z_{ij} \geq 1) = 1 - a = 50\%$ (E11.5 barcoding, Extended Data Fig. 6). To probe heterogeneity between single-cell expansions across cords, we allow that $\mathbb{E}(Z_{ij}|i) = g_i$, where g_i is a (random) per-cord expansion; all cells of the same cord amplify with same mean g_i, but cells of different cords may be subject to varying mean expansions. Then, it follows that $\mathbb{E}(g_i) = \mu$ is specified, while $\mathrm{Var}(g_i) = \sigma^2$ expresses the level of cord expansion variation through the additional parameter σ. The homogeneous case is contained with $\sigma = 0$, and $\sigma \gg 0$ encodes heterogeneous expansion. Critically, this framework enables the derivation of means and variances of all involved quantities. We obtain the mean relation $\mathbb{E}(Y_i) = \mu\, \mathbb{E}(X_i)$ and a variance of tubule cells after elongation as

$$\mathrm{Var}(Y_i) = \mathbb{E}(X_i)\frac{\mu\,(a-1) + \,(\mu^2+\sigma^2)\,(a+1)}{1-a} + \mathbb{E}(X_i)^2\,\sigma^2 + (\mu^2+\sigma^2)\,\mathrm{Var}(X_i).$$

Hence, σ can be computed directly from the embryonic and adult CVs using

$$\sigma^2 = \frac{\mu\,(1 - a + \mu\,((1-a)\,\big(\mathrm{CV}(Y_i) - \mathrm{CV}(X_i)\big)\,\big(\mathrm{CV}(X_i) + \mathrm{CV}(Y_i)\big)\,\mathbb{E}(X_i) - (1+a)))}{1 + a + (1-a)\,(1 + \mathrm{CV}(X_i)^2)\,\mathbb{E}(X_i)}.$$

When inserting values of $\mu = 30$, $a = 0.5$, $\mathbb{E}(X_i) = 2000/11$, $\mathrm{CV}(X_i) = \mathrm{CV}_{\mathrm{E12.5/E13.5}} \approx 0.31$ and $\mathrm{CV}(Y_i) = \mathrm{CV}_{\mathrm{adult}} \approx 0.43$, we obtain $\sigma \approx 7.5$. This indicates substantial variation in cord expansion, with some cords expanding 20-fold, and others 40-fold, to have on average a 30-fold increase in cell numbers. In simulations, we parametrize the mean cord expansion by $g_i \sim \mathrm{Gamma}(\alpha, \theta) + 1$ (with shape α and scale θ) and set $\alpha = ((\mu - 1)/\sigma)^2$ and $\theta = (\mu - 1)/\alpha$, satisfying $\mathbb{E}(g_i) = \mu$ and $\mathrm{Var}(g_i) = \sigma^2$ as desired (Extended Data Fig. 8d, for an overall scheme). Thus, solely by comparing cell number variation in embryo and adult, we can specify a model for the expansion of the testis cords becoming elongated tubules at appropriate mean and variance levels.

As the barcoding data is not being used to set up the expansion model or specify σ, we wondered if a feature in that data allows to test the model. If the substantial heterogeneity in the effectively one-dimensional elongations were true, one would expect the following: On average, the barcode patches, created at cord formation, are more stretched out in longer tubules at their final length, while in less elongated tubules barcodes are compressed in a shorter length. Hence, we compared the mean barcode number in small fragments (that came preferentially from shorter tubules) vs. the mean barcode number in sub-fragments that are pieces of a long fragment (preferentially a long tubule); where both were subsampled to an identical fragment length distribution. Indeed, we observe a slight shift between these mean values in both mice (~0.3 barcodes in mouse 2), while (without fitting these data) the model predicts a similar shift (~0.2 for mouse 2; Extended Data Fig. 8e); in contrast, no shifts (for $\sigma = 0$) or drastic shifts of more than

one barcode ($\sigma \gg 7.5$) are possible. This independent feature in the barcoding data validates the determined level of cord variation of the expansion model with $\sigma \approx 7.5$.

e, Theory of patch length variation in adult homeostasis. We develop a theoretical view of the patch length variation that explains the increased stability of patches in the neighbour competition model (tubular geometry) compared to the global competition model (agnostic of spatial geometry). To that end we derive the time evolution of the coefficient of variation (CV, standard deviation divided by the mean) for typical patch lengths in both models.

In the global competition model birth (cell division) and death (here representing biological cell differentiation) events of stem cells are balanced out, on average, on the population level. As a model we used the critical birth-death process, with a birth rate λ equaling the death rate. The mean and variance of patch sizes ℓ_t over time t, starting with an initial size of $\ell_0 \geq 1$ cells, are known to be $\mathbb{E}(\ell_t) = \ell_0$ and $\mathrm{Var}(\ell_t) = 2\ell_0\lambda t$ (Bailey, 1964[56], Equations 8.54, 8.55, 8.58; Supplementary Equations a) with a probability of extinction as $p(\ell_t = 0) = (\lambda t/(1 + \lambda t))^{\ell_0}$. Hence, patch lengths under global competition vary as $\mathrm{CV}_{\mathrm{global}}(\ell_t) = \sqrt{2\lambda t/\ell_0}$.

In the neighbour competition model stem cell differentiation is compensated by the immediate division of neighbouring cell (semantically equivalent to a replacement of a cell by one of its neighbours). The model achieves the same differentiation output as the global competition model when such replacements happen with the same rate λ. Importantly, a patch of cells with the same clone identity maintains an unaltered size if replacements take place within the patch boundaries (cells replacing cells of same clone identity). Hence the evolution of the patch length is only driven by the stem cell dynamics

at the patch boundaries. On a one-dimensional lattice, we observe shifts of the left boundary with a rate λ, as the patch increases by one cell when its leftmost cell replaces its left neighbour (rate $\frac{\lambda}{2}$), and the patch shrinks by one when its leftmost cell is replaced by its left neighbour of a different clone identity (rate $\frac{\lambda}{2}$). With analogue dynamics at the right boundary, we obtain a total rate of 2λ, independent of the current patch length ℓ_t. Hence one realizes that the patch length ℓ_t is described by a time-continuous symmetric random walk with an absorbing state at $\ell = 0$ for patch extinction. The solution of this process is known as $p(\ell_t = \ell) = e^{-2\lambda t}\left(I_{\ell-\ell_0}(2\lambda t) - I_{\ell+\ell_0}(2\lambda t)\right)$ (for $\ell \geq 1$) and $p(\ell_t = 0) = 1 - e^{-2\lambda t}\sum_{\ell=1}^{2\ell_0} I_{\ell-\ell_0}(2\lambda t)$, where $I_\nu(x)$ is the modified Bessel function of first kind and ℓ_0 is the patch length at time $t = 0$ (Heathcote and Moyal, 1959[58]). The mean follows as $\mathbb{E}(\ell_t) = \ell_0$ (identical to a random walk without absorbing state). The variance is given by $\mathrm{Var}(\ell_t) \approx 2\lambda t$ for our typical parameter regime (low probabilities of patch extinction for neighbour regulation, see below). This implies that patch lengths under local neighbour competition vary as $\mathrm{CV}_{\mathrm{neighbour}}(\ell_t) = \sqrt{2\lambda t}/\ell_0$.

Critically, the variance under neighbour competition does not scale with the initial patch size, in contrast to the linear dependence under global competition. For typical parameters of $t = 365$ days, $\lambda = 1/(6\text{ days})$ and our inferred mean patch size of $\ell_0 \approx 150$ cells (Extended Data Fig. 10b), we obtain patch extinction probabilities as $p(\ell_t = 0) \approx 0.087$ (global) and $p(\ell_t = 0) \approx 1.9 \times 10^{-38}$ (neighbour); and hence, $\mathrm{CV}_{\mathrm{global}} \approx 0.90$ and $\mathrm{CV}_{\mathrm{neighbour}} \approx 0.07$. This explains the drastic differences in long-term patch stability between the two competition models. Of note, we may extrapolate to a human testis by estimating the size of adult patches that reach a similar stability over a comparable human life span. Assuming the same division rate of individual stem cells and considering $t = 50$ years, a CV of 7% is reached at $\ell_0 \approx 1050$, suggesting a seven

1344 times larger human stem cell pool of about 420,000 cells per testis.

1345